2020/06/22
Archive Hash: d6eabcc-D
Archive Date: 2020/06/21

Multi-differential Z+jets cross sections at 13 TeV

The CMS Collaboration

Abstract

A study of the production of Z bosons in association with jets, in proton-proton collisions at a centre-of-mass energy of 13 TeV is presented. This study considers Z bosons decaying to two charged leptons, either electrons or muons. The cross sections and their ratios are measured with data recorded by the CMS experiment at the LHC in 2016, corresponding to an integrated luminosity of 35.9 fb^{-1}. The cross sections are measured as a function of the transverse momentum of the Z boson, and jet transverse momentum and rapidity for the five highest transverse momentum jets. The jet multiplicity distribution is measured for up to eight jets. The scalar sum of the jet momenta, which quantifies the hadronic activity, is also studied. The measurements are unfolded to the stable particle level and compared with predictions from various Monte Carlo event generators, as well as with theoretical predictions at leading and next-to-leading order in perturbative QCD.

This box is only visible in draft mode. Please make sure the values below make sense.

PDFAuthor:	Semiray Girgis Chyla
PDFTitle:	Multi-differential Z+jets cross sections at 13 TeV
PDFSubject:	CMS
PDFKeywords:	CMS, physics, Z Boson, Drell-Yan

Please also verify that the abstract does not use any user defined symbols

1 Introduction

In proton collisions the production of the Z boson is dominated by the Drell-Yan mechanism, in which a quark and an antiquark from the incoming protons annihilate into a pair of leptons (e, μ) [1]. At the LHC, the Z boson is commonly produced with additional QCD radiation, providing a perfect testing ground for our theoretical understanding of both strong and electroweak physics in a hadronic environment. Specifically, selecting events in which the Z decays to to charged leptons $Z(\rightarrow \ell^+\ell^-)$ which is a well understood process allows a sensitive evaluation of the accuracy of perturbative QCD (pQCD) [2–4] predictions at the highest accessible energies and for a broad range of kinematic configurations.

A precise understanding of $Z(\rightarrow \ell^+\ell^-)$ process is also critical in other Standard Model (SM) measurements and searches for physics beyond the SM, where it is an important background to studies of Higgs boson production and searches for dark matter and supersymmetric particles. The clean and readily identifiable signature and large production rate of this process provide an opportunity to accurately constrain the parton distribution functions (PDFs) and also probe the strong coupling constant α_s.

In addition to these physics motivations, $Z(\rightarrow \ell^+\ell^-)+$ jets production serves as an important experimental benchmark. It is a key ingredient in calibrating several parts of the detector (for example the jet energy scale). Comparisons of the Z+jets measurements with the predictions from Monte Carlo (MC) based event generators and reliable higher-order theoretical calculations can be used to improve these predictions to give an accurate description of experimental measurements.

Differential cross sections for the production of Z bosons in association with hadronic jets have been previously reported by the ATLAS, CMS, and LHCb Collaborations in proton-proton (pp) collisions at centre-of-mass energies of 7 [5–8], 8 [9–11] and 13 [12, 13] TeV, and by the CDF and D0 Collaborations in proton-antiproton collisions at 1.96 TeV [14, 15].

This paper presents measurement of the cross sections for the production of Z bosons in association with jets where the Z boson decays into a pair of oppositely charged leptons. The measurements use data from pp collisions at $\sqrt{s} = 13$ TeV with an integrated luminosity of 35.9 fb^{-1} recorded in 2016 by CMS. The measurements from the electron and muon final states are combined. The Z boson is defined as a pair of oppositely charged electrons (electron and positron) or muons (muon and anti-muon) restricted with invariant mass between 71 and 111 GeV. This range balances the signal acceptance, rejection of background processes, and, relative fractions of Z boson and γ^* events. In this analysis, we update and expand upon the results obtained by the CMS Collaboration at $\sqrt{s} = 13$ TeV with a data sample corresponding to an integrated luminosity of 2.19 fb^{-1} collected in 2015. The luminosity recorded in 2016 is larger than that recorded in 2015 by more than a factor of 10 enabling measurements of events with up to 8 jets inclusively and 5 jets differentially. This can be compared to the 2015 CMS paper that presents measurements of events with up to 6 jets inclusively and 3 jets differentially.

Cross-sections are measured as functions of jet multiplicity (N_{jets}) and the individual jet kinematic variables, rapidity (y) and transverse momentum (p_{T}) where the jets are ordered by decreasing p_{T}. Jet kinematic variables are presented for events with 1, 2, 3, 4, 5 jets. The term "inclusive" is used to designate distributions for events with at least N jets and the term "exclusive" for distributions where the events exactly N jets. Furthermore, cross sections are measured as a function of the scalar sum of the jet transverse momenta (H_{T}) for events up to 5 energetic jets.

This paper is organized as follows: Section 2 briefly describes the CMS detector; Section 3 presents data and simulated samples used in this analysis; Section 4 discusses event reconstruction, object selection and corrections; Section 5 summarizes the observables; Section 6 discusses phenomenological models and theoretical calculations details; Section 7 contains information about background estimation; Section 8 describes the unfolding procedure; Section 9 evaluates the systematic uncertainties. Finally, Sections 10 and 11 present the results and summary.

2 The CMS Detector

The central feature of the CMS apparatus is a superconducting solenoid of 6 m internal diameter, providing a magnetic field of 3.8 T. Within the solenoid volume are a silicon pixel and strip tracker, a lead tungstate crystal electromagnetic calorimeter (ECAL), and a brass and scintillator hadron calorimeter (HCAL), each composed of a barrel and two endcap sections. Forward calorimeters extend the pseudorapidity coverage provided by the barrel and endcap detectors. Muons are detected in gas-ionization chambers embedded in the steel flux-return yoke outside the solenoid.

The silicon tracker measures charged particles within the pseudorapidity range $|\eta| < 2.5$. It consists of 1440 silicon pixel and 15 148 silicon strip detector modules. For non-isolated particles of $1 < p_{\mathrm{T}} < 10\,\mathrm{GeV}$ and $|\eta| < 1.4$, the track resolutions are typically 1.5% in p_{T} and 25–90 (45–150) μm in the transverse (longitudinal) impact parameter [16]

The ECAL consists of 75 848 lead tungstate crystals, which provide coverage in pseudorapidity $|\eta| < 1.48$ in a barrel region (EB) and $1.48 < |\eta| < 3.0$ in two endcap regions (EE). Preshower detectors consisting of two planes of silicon sensors interleaved with a total of $3X_0$ of lead are located in front of each EE detector. In the barrel section of the ECAL, an energy resolution of about 1% is achieved for unconverted or late-converting photons that have energies in the range of tens of GeV. The remaining barrel photons have a resolution of about 1.3% up to a pseudorapidity of $|\eta| = 1$, rising to about 2.5% at $|\eta| = 1.4$. In the endcaps, the resolution of unconverted or late-converting photons is about 2.5%, while the remaining endcap photons have a resolution between 3 and 4% [17]. When combining information from the entire detector, the jet energy resolution amounts typically to 15% at 10 GeV, 8% at 100 GeV, and 4% at 1 TeV, to be compared to about 40%, 12%, and 5% obtained when the ECAL and HCAL calorimeters alone are used.

Muons are measured in the pseudorapidity range $|\eta| < 2.4$, with detection planes made using three technologies: drift tubes, cathode strip chambers, and resistive plate chambers. Matching muons to tracks measured in the silicon tracker results in a relative transverse momentum resolution, for muons with $20 < p_{\mathrm{T}} < 100\,\mathrm{GeV}$, of 1.3–2.0% in the barrel and better than 6% in the endcaps. The p_{T} resolution in the barrel is better than 10% for muons with p_{T} up to 1 TeV [18]. In the region $|\eta| < 1.74$, the HCAL cells have widths of 0.087 in pseudorapidity and 0.087 in azimuth (ϕ). In the η-ϕ plane, and for $|\eta| < 1.48$, the HCAL cells map on to 5×5 arrays of ECAL crystals to form calorimeter towers projecting radially outwards from close to the nominal interaction point. For $|\eta| > 1.74$, the coverage of the towers increases progressively to a maximum of 0.174 in $\Delta\eta$ and $\Delta\phi$. Within each tower, the energy deposits in ECAL and HCAL cells are summed to define the calorimeter tower energies, subsequently used to provide the energies and directions of hadronic jets.

Events of interest are selected using a two-tiered trigger system [19]. The first level (L1), composed of custom hardware processors, uses information from the calorimeters and muon detectors to select events at a rate of around 100 kHz within a time interval of less than 4 μs. The second level, known as the high-level trigger (HLT), consists of a farm of processors running a version of the full event reconstruction software optimized for fast processing, and reduces the event rate to around 1 kHz before data storage. A more detailed description of the CMS detector, together with a definition of the coordinate system used and the relevant kinematic variables, can be found in Ref. [20].

3 Event Samples

The data sample analyzed corresponds to an integrated luminosity of $35.9\,\mathrm{fb}^{-1}$, collected in 13 TeV pp collisions with the CMS detector during the 2016 data taking period. Candidate events are selected online using single-lepton triggers, which require at least one isolated electron (muon) with $p_{\mathrm{T}} > 25(24)$ GeV and $|\eta^{l}| < 2.4$. The total trigger efficiency for events within the acceptance of this analysis is greater than 90%. Simulated events for both signal and background are produced using various Monte Carlo (MC) event generators, with the CMS detector response modeled using the GEANT4 [21] program. These events are then reconstructed using the same algorithms that are used to reconstruct collision data and are normalized to the integrated luminosity of the data sample using their respective cross sections. For the simulation of the signal, we use a sample generated with MADGRAPH5_aMC@NLO (MG5_aMC) [22] using the FxFx merging scheme [23]. Parton showering and hadronization are simulated with PYTHIA8 [24] using the CUETP8M1 tune [25]. The matrix element includes Z + 0,1,2 jets at Next-to-Leading-Order (NLO), giving a Leading Order (LO) accuracy for Z + 3 jets.

The production of $\mathrm{Z}(\rightarrow \ell^{+}\ell^{-}) +$ jets can be mimicked by various background sources:Top quark pair production ($\mathrm{t\bar{t}}$) events, diboson (WW, WZ, ZZ), triboson (ZZZ, WWZ,WZZ) production, and W bosons produced in association with jets, as well as Z + jets events in which the Z boson decays into $\mathrm{Z} \rightarrow \tau^{+}\tau^{-}$. Background processes are split into two components: the resonant and nonresonant background. Resonant background comes from events with a real Z boson in the final state (WZ, ZZ, tribosons, etc.) and it is estimated using MC samples. The nonresonant background comes from events that do not have a Z boson in the final state ($\mathrm{t\bar{t}}$) and it is estimated using events with both an electron and muon. $\mathrm{Z} \rightarrow \tau^{+}\tau^{-}$ events are considered background and are estimated using the MG5_aMC signal sample.

Background samples corresponding to electroweak diboson production [26] are generated at NLO with POWHEG [27–30] interfaced to PYTHIA 8 or MG5_aMC interfaced to PYTHIA 8. The backgrounds from tribosons are generated at NLO using MG5_aMC interfaced with PYTHIA 8. All samples are normalized to their cross sections calculated at NLO.

The simulated event samples include multiple pp collisions within a bunch crossing (pileup). Simulated events are reconstructed and analyzed in the same way as collision events, subject to additional corrections that account for differences between data and simulation in trigger, selection efficiencies, and in the pileup interactions. The differences between data and simulation in the pileup conditions results to a different vertex multiplicity and also differences in other pileup sensitive observables such as rho and sumET.

4 Event Reconstruction, Object Selection and Corrections

The global event reconstruction (also called particle-flow event reconstruction [31]) aims to reconstruct and identify each individual particle in an event, with an optimized combination of all subdetector information. In this process, the identification of the particle type (photon, electron, muon, charged hadron, neutral hadron) plays an important role in the determination of the particle direction and energy.

The reconstructed vertex with the largest value of summed physics-object p_{T}^2 is taken to be the primary pp interaction vertex. The physics objects are the jets, clustered using the jet finding algorithm [32, 33] with the tracks assigned to the vertex as inputs, and the associated missing transverse momentum, taken as the negative vector sum of the p_{T} of those jets.

Electron candidates are reconstructed by combining the information from the ECAL and from the silicon tracker. The energy of electrons is determined from a combination of the electron momentum at the primary interaction vertex as determined by the tracker, the energy of the corresponding ECAL cluster, and the energy sum of all bremsstrahlung photons spatially compatible with originating from the electron track. The Super Cluster reconstruction efficiency for $E_T^{SC} > 5$ GeV is close to 100%. The momentum resolution for electrons with $p_{\mathrm{T}} \approx 45$ GeV originating from $\mathrm{Z}(\to e^+e^-)$ decays ranges from 1.7% to 4.5%. It is generally better in the barrel region than in the endcaps, and depends on the bremsstrahlung energy emitted by the electron, as it traverses the material in front of the ECAL [34]. To reduce the electron misidentification rate, electron candidates are subject to additional identification criteria that are based on the distribution of the electromagnetic shower in the ECAL, a matching of the trajectory of an electron track with the cluster in the ECAL, and consistency of the track with originating from the selected primary vertex. Muon candidates are reconstructed with a global fit using both the inner tracking system and the muon spectrometer [18]. The momentum of the muons is obtained from the curvature of the corresponding track. Muons are selected as Z decay product candidates from the particle flow (PF) objects. The efficiency of the muon reconstruction algorithm is higher than 0.95% for muons with $p_{\mathrm{T}} > 20\,\mathrm{GeV}$. The relative p_{T} resolution at 100 GeV is 2% in the barrel and 6% in the endcap and increases to 10% in the endcap at 1 TeV.

Jets are formed from the particles reconstructed by the PF algorithm, using the FAST-JET software package and the anti-k_{T} jet clustering algorithm [35] with a distance parameter of 0.4. The jet four-momentum is defined as the vector sum of the four-momenta of its constituents. The technique of charged-hadron subtraction [36] is used to reduce the pileup contribution by removing charged particles that originate from pileup vertices. The jet four-momentum is corrected for the difference observed in the simulation between jets built from PF candidates and generator-level particles. The jet mass and direction are kept constant when the corrections are applied. An offset correction is applied to jet energies to take into account the contribution from additional pp interactions within the same or nearby bunch crossings. Further jet energy corrections are applied for differences between data and simulation in the pileup in zero-bias events and in the p_{T} balance in dijet, Z + jet, and γ + jet events. To maximize the reconstruction efficiency while reducing the instrumental background and contamination from pileup jets, tight identification quality criteria are applied to jets, based on the fraction of energy carried by charged and neutral hadrons, and by charged leptons and photons. A minimum threshold of 30 GeV on the p_{T} of jets is required to ensure that they are well measured and to reduce the pileup contamination. Jets are required to have $|\eta| < 2.4$ and to be separated from all selected lepton candidates by at least $R \leq 0.4$.

To compare the measured distributions with the theoretical predictions, various experimental corrections are applied after subtracting the total expected background from the observed number of events in each bin. A correction for detector resolution effects is implemented using an unfolding technique (see details in section 8). The event acceptance and selection efficiency are estimated using simulation and are used to correct the data. To correct for differences in efficiencies between data and simulation for lepton reconstruction, identification, isolation, and trigger, efficiency corrections are determined from the data using the tag-and-probe method [37].

We select events with one isolated electron (muon) with transverse momentum of at least 25 (24) GeV. After offline reconstruction, two leptons are required with the first having $p_{\mathrm{T}} > 30\,\mathrm{GeV}$ and the second having $p_{\mathrm{T}} > 20\,\mathrm{GeV}$. We require that the two electrons (muons) with highest transverse momenta form a pair of oppositely charged leptons with an invariant mass in the range $91 \pm 20\,\mathrm{GeV}$. Electron candidates are required to be reconstructed within $|\eta| < 2.4$, excluding the barrel-to-endcap ($1.444 < |\eta| < 1.566$) transition regions of the ECAL. Electrons and muons are considered isolated based on the scalar p_{T} sum of the nearby PF candidates with a distance $R = \sqrt{(\Delta\eta)^2 + (\Delta\phi)^2} < 0.4$. For both electrons and muons medium identification criteria is applied. To correct misalignment of the CMS detector in both data and MC for the muon channel, corrections [38] are applied.

5 Observables

In this paper, the cross sections are presented as functions of several kinematic and angular observables to characterize the production mechanisms of $\mathrm{Z}(\rightarrow \ell^+\ell^-) +$ jets events. The cross section has been measured as a function of both the exclusive and inclusive jet multiplicities up to a total number of either jets in the final state. In addition, it has been measured as a function of the kinematic variables, p_{T}, y and H_{T} for individual jets for N_{jets} from 1 to 5.

Comparisons of jet multiplicity distributions with the predictions of different MC generators give a general idea of how accurately these generators describe different jet configurations.

The measurement of the distribution of $p_{\mathrm{T}}(Z)$ for events with at least one jet is vital to understand the balance of the transverse momentum between the jets and the Z boson, and can be used for comparing theoretical predictions which achieve multiple soft-gluon emissions with different ways.

The (y) of Z boson ($y(Z)$) is related to the momentum fraction (x) carried by the parton in the forward-going (backward-going) proton. Therefore, the y distribution directly reflects the PDFs of the interacting partons. At the LHC, the $y(Z)$ distribution is expected to be symmetric around zero, therefore the appropriate measurement is the distribution of Z bosons as a function of the $|y|$.

The jet kinematic variables and H_{T} are sensitive to the effects of higher order corrections and these variables make it possible to specify the level of agreement between data and theory.

In terms of angular correlations between jets, cross sections are measured as a function of the difference rapidity in $\Delta y(j_i,j_k)$, and of the difference in azimuthal angle $\Delta\phi(j_i,j_k)$, between the i^{th} and k^{th} jets from the p_{T}-ordered list of jets in the event. For angular correlations between Z boson and jets, cross sections are measured as a function of the difference and sum in $\Delta y(Z,j_k)$, and of the difference in azimuthal angle $\Delta\phi(Z,j_k)$. The azimuthal angular separation ($\Delta\phi$) between the final state Z boson and jet is sensitive to the soft gluon radiation. The advantage of studying the ϕ distribution is that it only depends on the directions of the final state Z boson and jet.

Lastly, double differential cross sections are measured as functions of leading jet p_{T} and y, leading jet and $y(Z)$, $p_{\mathrm{T}}(Z)$ and y. The measured cross sections are corrected for detector effects and compared with theoretical predictions to LO and NLO matched with parton showering as implemented in MC generators.

6 Phenomenological Models and Theoretical Calculations

We compare the measured Z + jets differential cross sections to three calculations: MG5_AMC at NLO, MG5_AMC at LO, and the GENEVA MC program. The two MG5_AMC calculations (version 2.2.2) [39] are interfaced with PYTHIA 8 (version 8.212) [40]. For the LO MG5_AMC, the generator calculates LO Matrix Elements (MEs) for five processes: pp $\rightarrow$ Z + Njets with $N = 0...4$. The NNPDF 3.0 LO PDF [41] is used and $\alpha_S(m_Z)$ is set to 0.130. The NLO MG5_AMC prediction includes NLO ME calculations for pp $\rightarrow$ Z + Njets with N up to 2. The NNPDF 3.0 NLO PDF is used and $\alpha_S(m_Z)$ is set to 0.118. Both predictions use PYTHIA 8 to model the initial+final state parton showers and hadronization with the CUETP8M1 [42] tune that includes the NNPDF 2.3 [43] LO PDF and $\alpha_S(m_Z)$ = 0.130. ME and parton shower matching is done using the k_T-MLM [22, 44] scheme with the matching scale set at 19 GeV for the LO MG5_AMC and the FxFx [45] scheme with the matching scale set to 30 GeV for the NLO MG5_AMC.

In this analysis uncertainties in the ME calculation for the NLO MG5_AMC prediction are estimated using the procedure recommended by the authors of the generator. Fixed-order cross section calculations depend on the renormalization (μ_R) and factorization (μ_F) scales. The uncertainty coming from missing terms in the fixed-order calculation is estimated by varying the μ_R and μ_F scales by factors of 0.5 and 2. Uncertainties in PDF and α_S values are also estimated in the case of the FxFx-merged sample. The PDF uncertainty is estimated using the set of 100 replicas of the NNPDF 3.0 NLO PDF, and the uncertainty in the α_S value used in the ME calculation is estimated by varying it by ± 0.001. These two uncertainties are added in quadrature to the ME calculation uncertainties. All these uncertainties are obtained using the reweighting method [46] implemented in these generators.

7 Background Estimation

Background events are split into two categories: resonant and non-resonant. The resonant background, which consists mainly of multi-boson events with at least one Z boson in the final state, are estimated using MC samples. The non-resonant events contain two leptons primarily from W decays, such as $t\bar{t}$, and are estimated from a data-driven method. The decay $Z \rightarrow \tau^+\tau^-$ is considered a background and is estimated from the MG5_AMC signal MC sample.

The data driven method for the non-resonant background uses a control region containing events with one electron and muon ($e^\pm\mu^\mp$) passing all other signal region criteria. The control region is then used to estimate the non-resonant background in the signal region by applying a conversion factor to account for cross section and lepton efficiency differences. Assuming lepton flavor symmetry, the cross section for a $e^\pm\mu^\mp$ final state and a e^+e^- or $\mu^+\mu^-$ final state differs only by a factor of 2. The difference in efficiency between muons and electrons is estimated using the total yields of the two channels. Resonant signal and background are estimated in the control region by the same signal MC and subtracted to avoid double counting.

Measurements of jet multiplicity and the kinematics of the Z boson and leading get are show in figures 1 - 3 together with the results of the simulation. The fraction of background events is small compared to the signal and amounts to approximately 1% for $\geq$0 jets increasing to 10% at 5 or more jets. For transverse momentum variables the background increases from 1% below 100 GeV to 10% in the high-pt tails.

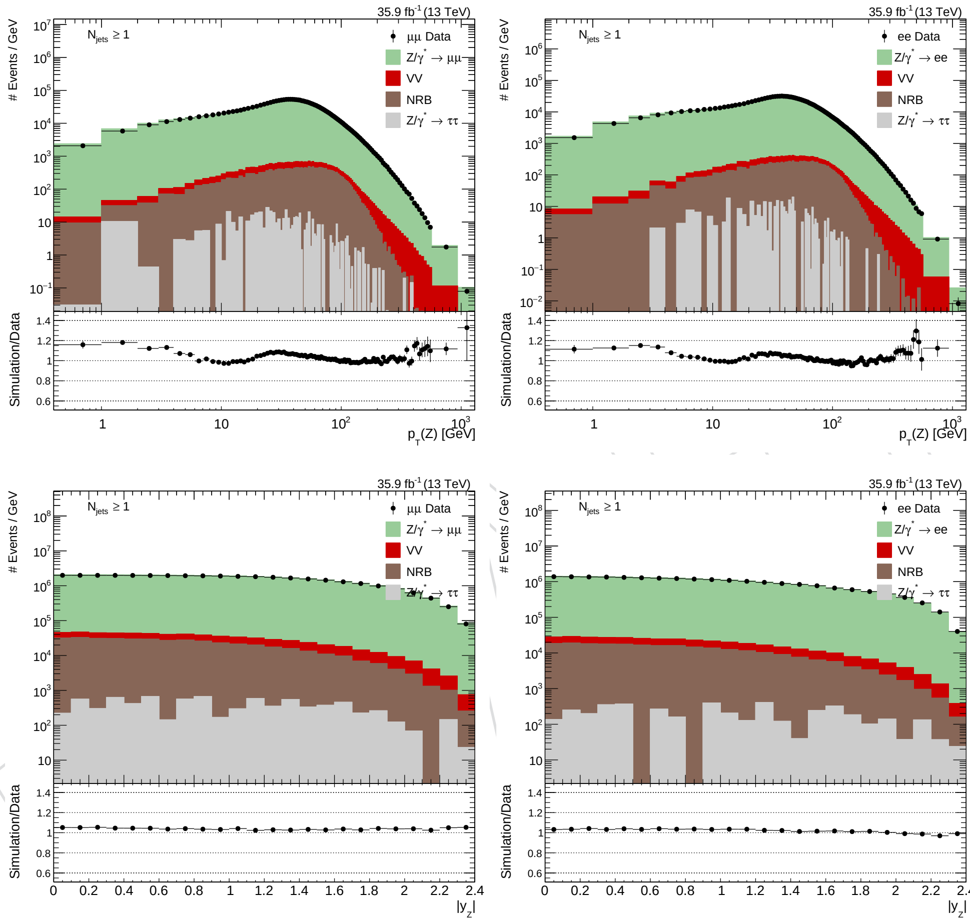

Figure 1: Z candidate p_T (upper) and $|y|$ (lower) with at least one jet for the electron (left) and muon (right) channel. The background is estimated from both simulation and data driven methods describe in section 7. The ratio shows the combined statistical uncertainty of the data and total simulation.

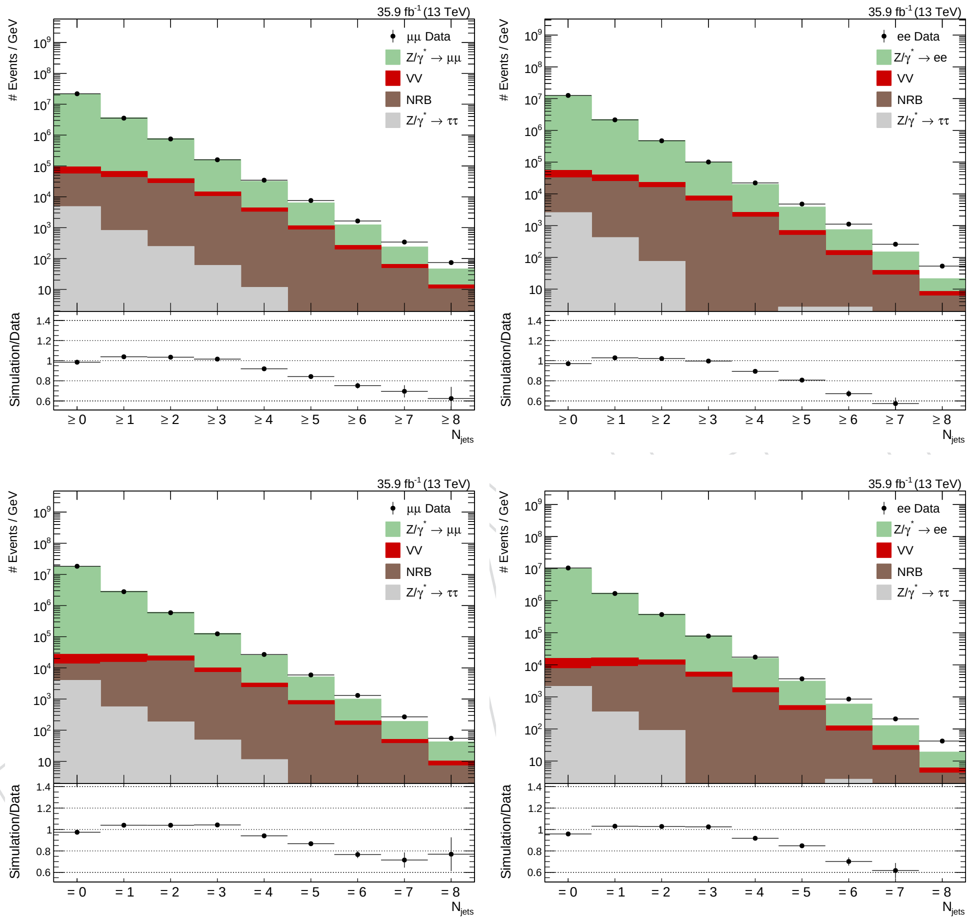

Figure 2: Inclusive (upper) and exclusive (lower) jet multiplicity for the electron (left) and muon (right) channel. The background is estimated from both simulation and data driven methods describe in section 7. The ratio shows the combined statistical uncertainty of the data and total simulation.

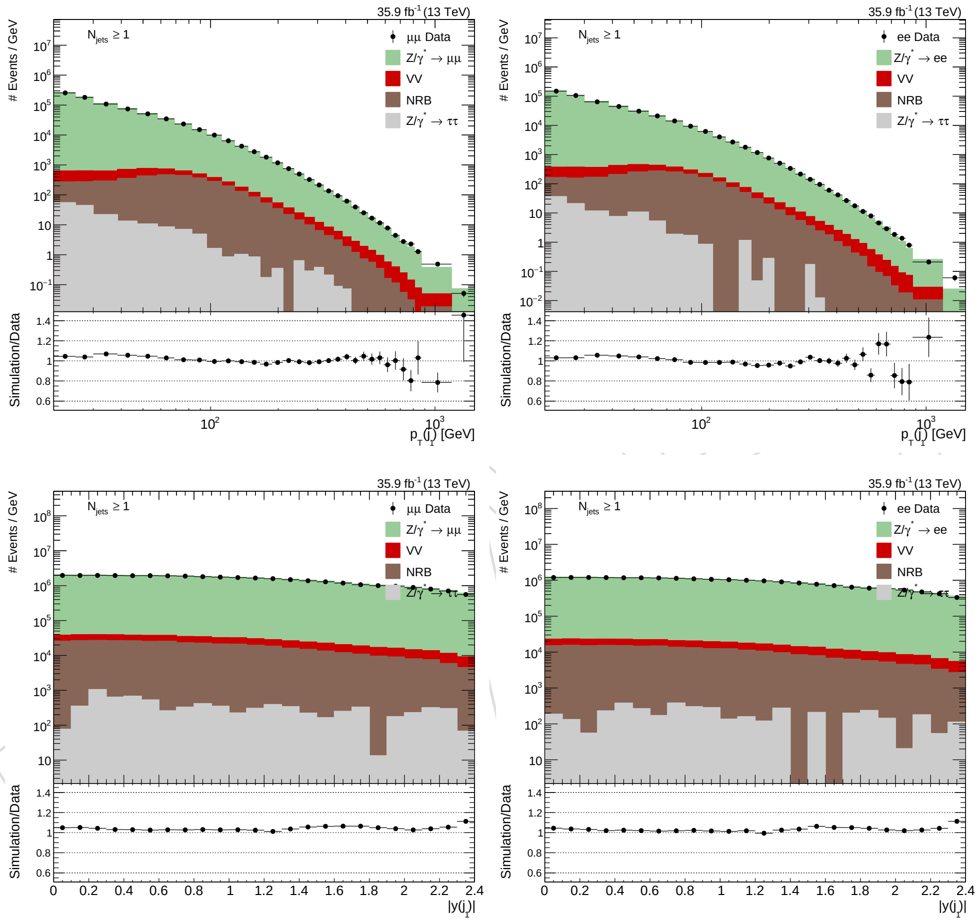

Figure 3: First jet p_T (upper) and $|y|$ (lower) for the electron (left) and muon (right) channel. The background is estimated from both simulation and data driven methods describe in section 7. The ratio shows the combined statistical uncertainty of the data and total simulation.

8 Unfolding Procedure

In this analysis unfolding is performed to remove detector effects and estimate the particle (or generator) level distributions in data. The MADGRAPH5_aMC@NLO MC sample is used to extract the detector transformation, called the response matrix, that feeds into the unfolding algorithm. For each distribution the contributions from background and fakes are subtracted from data prior to unfolding. Fakes are defined as jets that exist at the reconstruction level but do not have a particle level counterpart and are assumed to come from processes such as clustering pile-up particles into a jet. The fakes are estimated from MC by calculating the difference in the number of events between a reconstruction level bin and the sum of all generator level events in the same reconstruction bin. The unfolding procedure consists of performing a least-squares fit with optional Tikhonov regularization [47], as implemented in the TUnfold software package [48]. In this analysis variables associated with angles such as η and $|y|$ are unfolded without regularization while the momentum variable needs some regularization. The best value for the regularization parameter is chosen using the well-established L-curve method [49]. Closure tests are performed by checking the re-folded distributions with the original data.

The particle level objects are defined to be particles with a lifetime of $c\tau > 1\,\mathrm{cm}$ (excluding neutrinos) and identified using the same algorithms as used for the data. In addition, leptons are stable particle from Z decays, dressed by adding the momenta of all photons within $\Delta R < 0.1$ from their directions. The momenta of the leading leptons are summed to obtain the particle level Z momentum. The particle level objects are required to pass the same kinematic selections as at detector level.

9 Systematic Uncertainties

The sources of experimental uncertainties are divided into the following categories: Jet energy scale (JES) and jet energy resolution (JER), lepton efficiencies (identification, isolation, and track reconstruction), lepton energy scale (LES) and resolution (LER), trigger efficiency, luminosity, pileup, background and unfolding uncertainties. The uncertainties listed above are assumed to be independent such that each can be computed individually and added in quadrature to obtain a total uncertainty. To compute the systematic uncertainty from each source, the analysis is repeated using the source values increased and decreased by 1σ from the central value. This results in bin-by-bin uncertainty contributions from each source in the unfolded distributions.

The JES uncertainty originates mainly from the uncertainty on the single particle response and it is the dominant source of systematic uncertainty. It affects both the reconstruction of the transverse energy of the selected jets and also the reconstructed kinematic variables measured with the calorimeter. In this analysis jet energy corrections (JEC) were applied to take into account inefficiencies, non-linearities and finite resolution in energy and position of the reconstructed jets. The effect of the JES uncertainty is studied by scaling up and down the reconstructed jet energy by p_{T} and η-dependent scale factors. A similar procedure is followed for the JER. The uncertainties due to the JES and the JER vary from 1-11% as a function of jet multiplicity.

Scale factors for lepton efficiencies are applied on an object-by-object basis so that the simulation samples reflect the inefficiencies observed in data. The lepton identification, isolation, track reconstruction and trigger efficiencies in simulation are corrected with scaling factors derived with a tag-and-probe method and applied as a function of lepton p_{T} and η. To estimate the uncertainties, the total yield is recomputed with the scaling factors varied up and down by the fit uncertainties. The uncertainties associated with lepton efficiency in the electron channel is 1% while in the muon channel 0.5%.

The LES and LER uncertainties make a small contribution to the overall lepton uncertainties of ∼1% for each channel.

A normalization uncertainty is assigned to the imperfect knowledge of the integrated luminosity. This is applied as an overall normalization uncertainty on all processes stemming from MC simulation and takes a value of 2.5% [50].

To match the pileup conditions in data and in MC simulation, pileup reweighing is applied to the simulated samples. The reweighting factors depend on the minimum-bias cross section. We vary the nominal minimum-bias cross section of 69.2 mb up and down by its uncertainty of 4.6% when reconstructing the response matrices, and take the difference in the unfolded data as the uncertainty.

The uncertainty on the unfolding procedure is due to both the statistical uncertainty in the response matrix coming from the finite size of the MC sample used to compute it and to the possible event generator dependence of the response matrix itself. Because of the finite binning a different distribution will lead to a different response matrix. This uncertainty is estimated by weighting the MC to agree with the data in each distribution and building a new response matrix. The weighting is done using a finer binning than for the measurement. The difference between the nominal results and the results unfolded using the alternative response matrix is taken as the systematic uncertainty. An additional uncertainty comes from the finite size of the MC sample used to build the response matrix. This source of uncertainty is called unfolding statistics ("unf stat") and is included in the systematic uncertainty of the measurement as well. Statistical fluctuations in the response matrix are propagated analytically in the TUnfold package.

Lastly, the background samples are varied by their corresponding cross section uncertainty before being subtracted from data prior to unfolding. The systematic uncertainties used for the combination of the electron and muon channels are summarized in Tables 1 - 5.

10 Results

The measurements from the electron and muon channels are consistent within the statistical and systematic uncertainties, and hence they are combined. To combine the two channels, a hybrid method based on the weighted mean and the best linear unbiased estimates (BLUE) method [51, 52] is used to calculate the cross section values. This method requires the construction of a covariance matrix (including statistical and systematic uncertainties) with all correlations determined externally.

The size of the 2016 data samples allows us to determine the differential cross sections of jet multiplicities up to eight jets and to study the cross sections as a function of several kinematic observables up to five jets. The combined single-differential cross sections are shown in figures 4-22, while double-differential cross sections are given in figure 23-25. All results are compared with theoretical predictions from MG5_aMC at LO and MG5_aMC at NLO and compared to the GENEVA MC program for results with at least one or two jets.

The jet transverse momenta and rapidities up to five leading jets can be seen in figure 4-8. For both quantities data distributions are well reproduced by the simulations. The MG5_aMC at LO and, MG5_aMC at NLO, describe the data well in general. The GENEVA prediction shows good agreement for the measured p_{T} and y of the first jet, while it undershoots the data at low

p_T for the second jet.

In addition, the inclusive jet differential cross sections as a function of H_T for events with at least one, two and three jets respectively are presented in figure 9. Both MG5_AMC at LO and MG5_AMC at NLO are compatible with the measurement. The contribution at higher values of H_T is slightly overestimated, but the discrepancy is compatible with the theoretical and experimental uncertainties. The slopes of the distributions for the first two jet multiplicities predicted by the GENEVA samples do not fully describe the data.

In figure 12 the measured cross sections as a function of the exclusive jet multiplicity, for a total number of up to 8 jets in the final state, are shown. The trend of the jet multiplicity represents the expectation of the pQCD prediction for an exponential decay with the number of jets. The agreement is very satisfactory for the exclusive distributions for all the theoretical estimations, within the uncertainties and going up to the maximum number of final state partons included in the ME, namely 4 in the MC generators used here. The GENEVA predictions do not model the jet multiplicity for events with greater than 2 jets.

Above the jet cut of 30 GeV the $p_T(Z)$ distribution in figure 12 is described well where the kinematics are dominated by jets modeled at NLO accuracy. Below the jet cut of 30 GeV non-perturbative QCD effects become dominant and the predictions show significant deviations from data. In many regions the total uncertainty in data is smaller than the theoretical uncertainty and greatly reduces the predictive power of the sample.

The results for the double-differential cross sections are presented in figures 23 - 25 and are compared to the predictions described in Section 6. The double differential cross sections are shown for at least one jet as a function of leading jet p_T and rapidity (Figure 23), leading jet and Z boson rapidity (Figure 24), Z boson p_T and rapidity (Figure 25). In Figure 25, predicted spectrums differ from the measurement, showing a steeper slope in the low p_T region. In general, all the predictions are in agreement with data and the NLO prediction provides a better description than LO and GENEVA for double differantial cross sections.

Overall the MG5_AMC at NLO predictions describe the data within theoretical uncertainties over a range of kinematic variables. In regions of NLO accuracy, such as the first and second jet p_T and y, the agreement is within 10% up to the TeV scale.

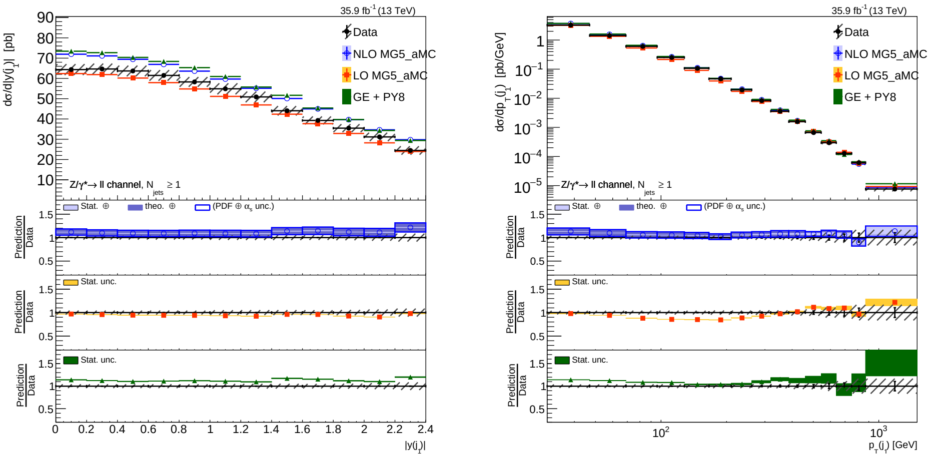

Figure 4: The measured differential cross section as a function of leading jet $|y|$ (left) and p_T (right) with at least one jet for the combined channel. For data the black bars show the statstical uncertainty and the hashed area shows the total uncertainty. The measurement is compared to NLO MG5_AMC, LO MG5_AMC, and GENEVA. The uncertainty for predictions is shown only in the ratio plots with statistical, PDF, and scale uncertainties for the NLO MG5_AMC and statistical only for the GENEVA and LO MG5_AMC predictions.

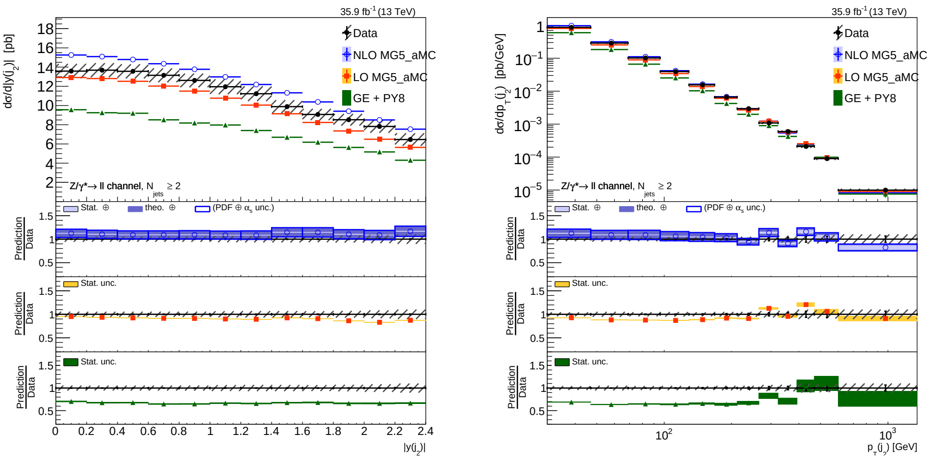

Figure 5: The measured differential cross section as a function of second jet $|y|$ (left) and p_T (right) with at least two jets for the combined channel. For data the black bars show the statstical uncertainty and the hashed area shows the total uncertainty. The measurement is compared to NLO MG5_AMC, LO MG5_AMC, and GENEVA. The uncertainty for predictions is shown only in the ratio plots with statistical, PDF, and scale uncertainties for the NLO MG5_AMC and statistical only for the GENEVA and LO MG5_AMC predictions.

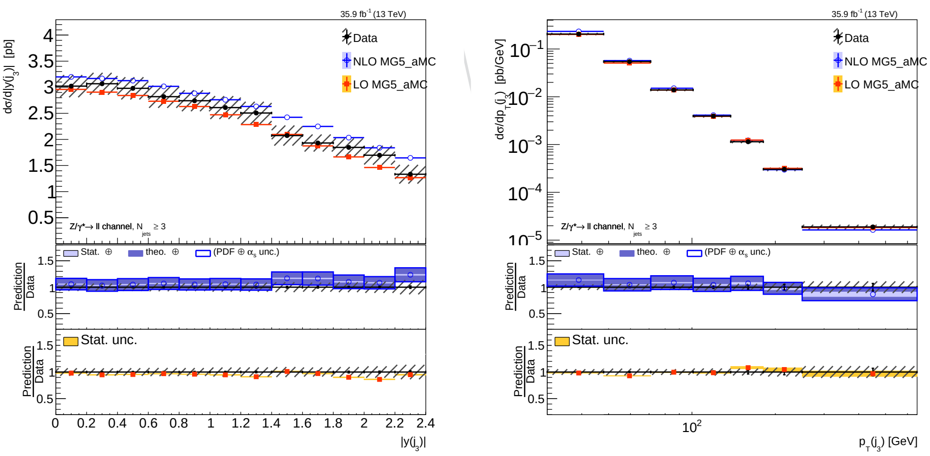

Figure 6: The measured differential cross section as a function of third jet $|y|$ (left) and p_T (right) with at least three jets for the combined channel. For data the black bars show the statstical uncertainty and the hashed area shows the total uncertainty. The measurement is compared to NLO MG5_AMC and LO MG5_AMC. The uncertainty for predictions is shown only in the ratio plots with statistical, PDF, and scale uncertainties for the NLO MG5_AMC and statistical only for the LO MG5_AMC predictions.

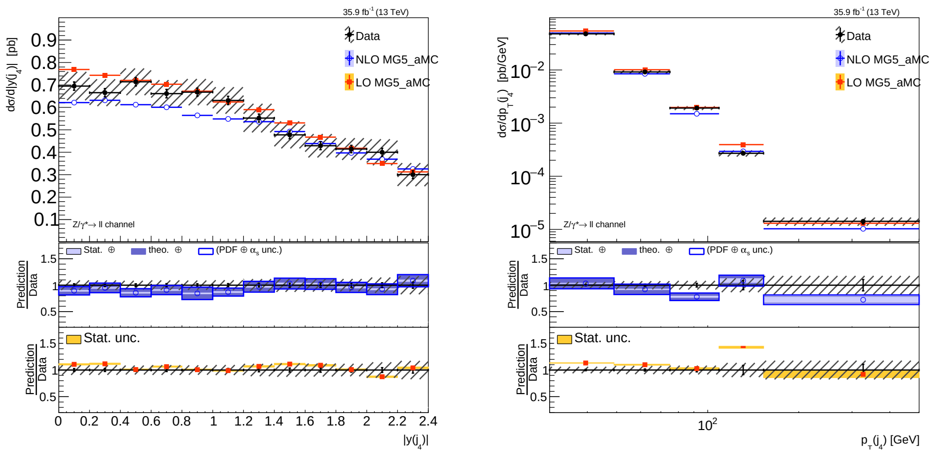

Figure 7: The measured differential cross section as a function of fourth jet $|y|$ (left) and p_T (right) with at least four jets for the combined channel. For data the black bars show the statstical uncertainty and the hashed area shows the total uncertainty. The measurement is compared to NLO MG5_AMC and LO MG5_AMC. The uncertainty for predictions is shown only in the ratio plots with statistical, PDF, and scale uncertainties for the NLO MG5_AMC and statistical only for the LO MG5_AMC predictions.

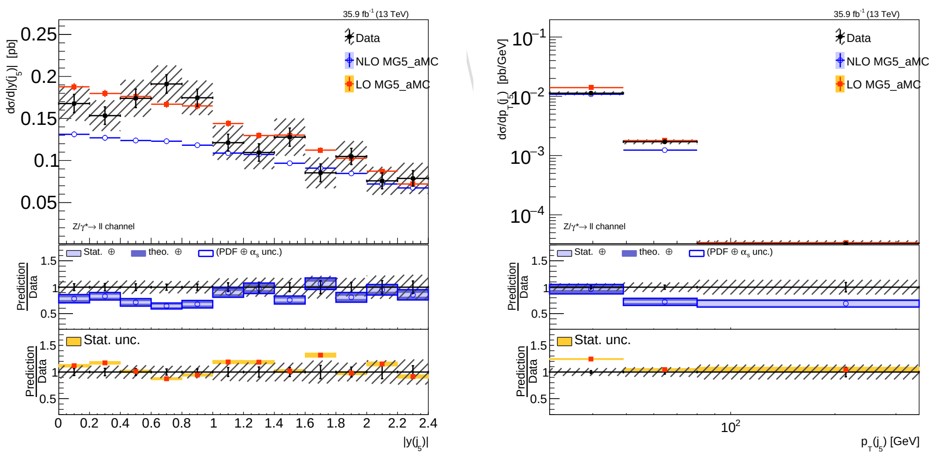

Figure 8: The measured differential cross section as a function of fifth jet $|y|$ (left) and p_T (right) with at least five jets for the combined channel. For data the black bars show the statstical uncertainty and the hashed area shows the total uncertainty. The measurement is compared to NLO MG5_AMC and LO MG5_AMC. The uncertainty for predictions is shown only in the ratio plots with statistical, PDF, and scale uncertainties for the NLO MG5_AMC and statistical only for the LO MG5_AMC predictions.

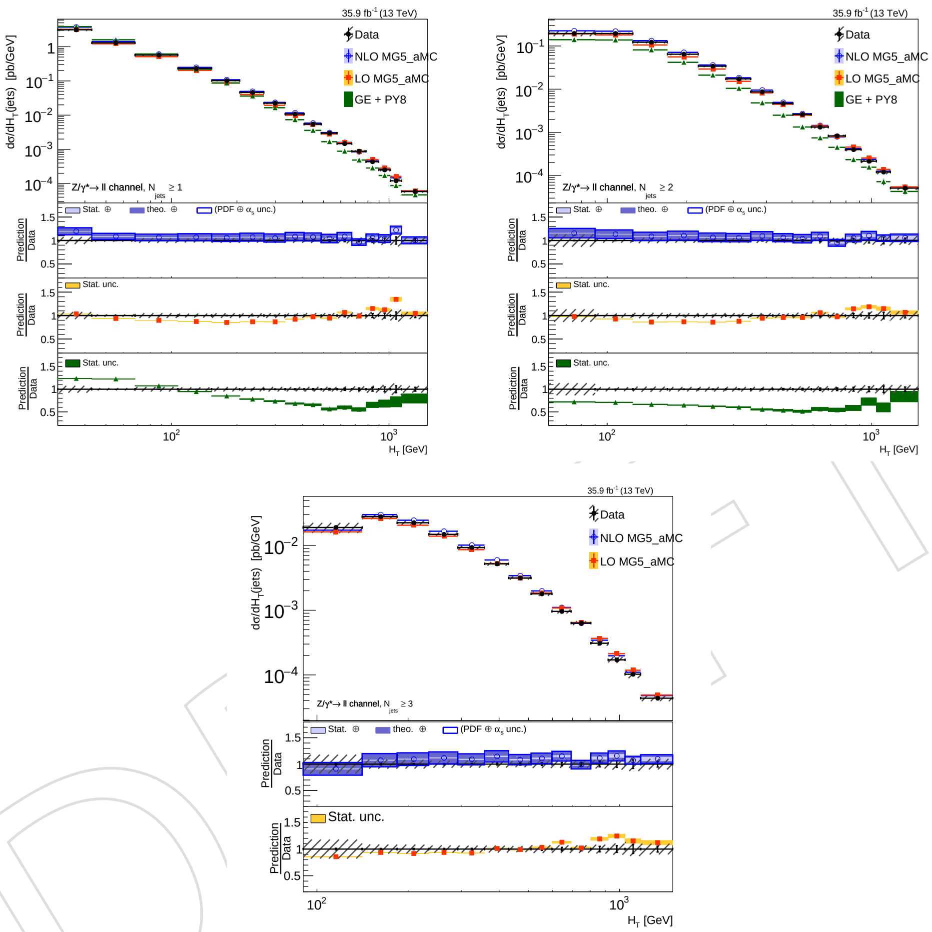

Figure 9: The measured differential cross section as a function of total hadronic p_T with at least one(left), two(middle), and three(right) jets. For data the black bars show the statstical uncertainty and the hashed area shows the total uncertainty. The measurement is compared to NLO MG5_AMC and LO MG5_AMC. The measurements with at least one and two jets is also compared to GENEVA. The uncertainty for predictions is shown only in the ratio plots with statistical, PDF, and scale uncertainties for the NLO MG5_AMC and statistical only for the GENEVA and LO MG5_AMC predictions.

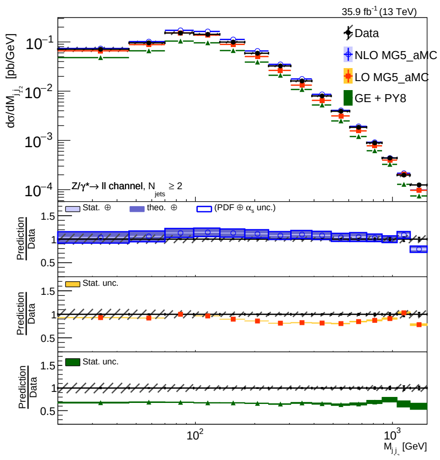

Figure 10: The measured differential cross section as a function of dijet mass with at least two jets. For data the black bars show the statstical uncertainty and the hashed area shows the total uncertainty. The measurement is compared to NLO MG5_AMC, LO MG5_AMC, and GENEVA. The uncertainty for predictions is shown only in the ratio plots with statistical, PDF, and scale uncertainties for the NLO MG5_AMC and statistical only for the GENEVA and LO MG5_AMC predictions.

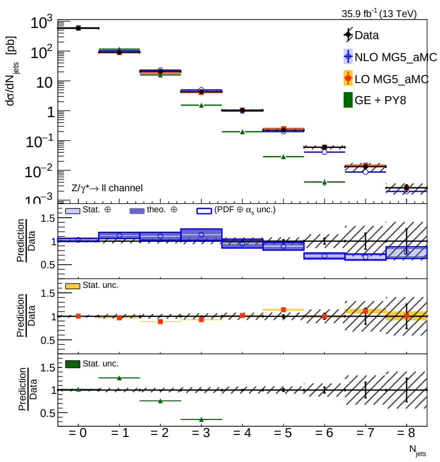

Figure 11: The measured differential cross section as a function of exclusive jet multiplicity. For data the black bars show the statstical uncertainty and the hashed area shows the total uncertainty. The measurement is compared to NLO MG5_AMC, LO MG5_AMC, and GENEVA. The uncertainty for predictions is shown only in the ratio plots with statistical, PDF, and scale uncertainties for the NLO MG5_AMC and statistical only for the GENEVA and LO MG5_AMC predictions.

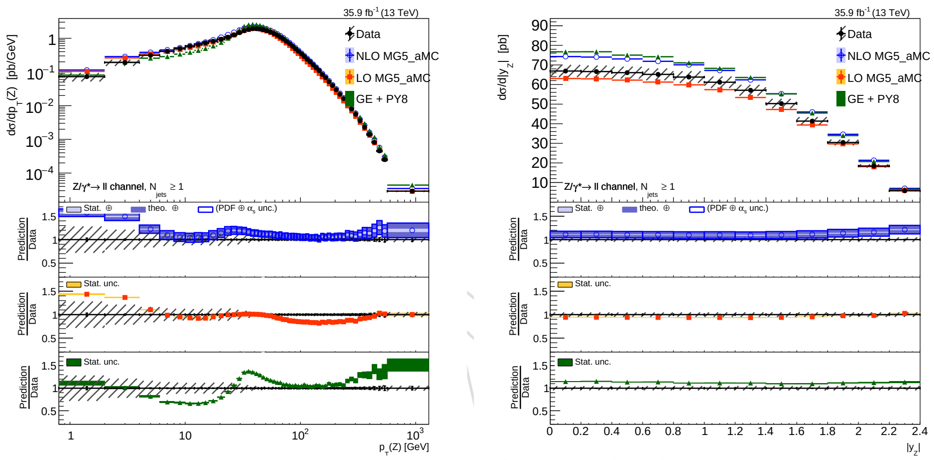

Figure 12: The measured differential cross section as a function of Z candidate p_T (left) and Z absolute rapidity (right) with at least one jet. For data the black bars show the statstical uncertainty and the hashed area shows the total uncertainty. The measurement is compared to NLO MG5_aMC, LO MG5_aMC, and GENEVA. The uncertainty for predictions is shown only in the ratio plots with statistical, PDF, and scale uncertainties for the NLO MG5_aMC and statistical only for the GENEVA and LO MG5_aMC predictions.

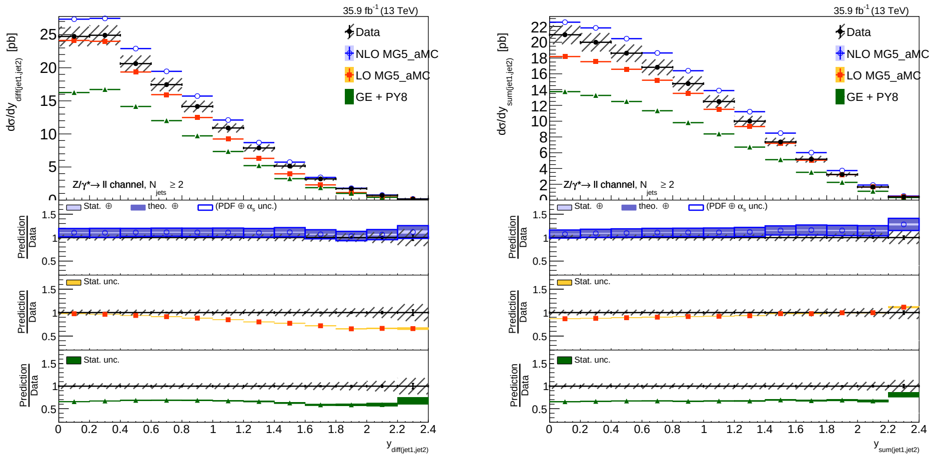

Figure 13: The measured differential cross section as a function of the leading and subleading jet rapidity difference(left) and sum(right) with at least two jets. For data the black bars show the statstical uncertainty and the hashed area shows the total uncertainty. The measurement is compared to NLO MG5_AMC, LO MG5_AMC, and GENEVA. The uncertainty for predictions is shown only in the ratio plots with statistical, PDF, and scale uncertainties for the NLO MG5_AMC and statistical only for the GENEVA and LO MG5_AMC predictions.

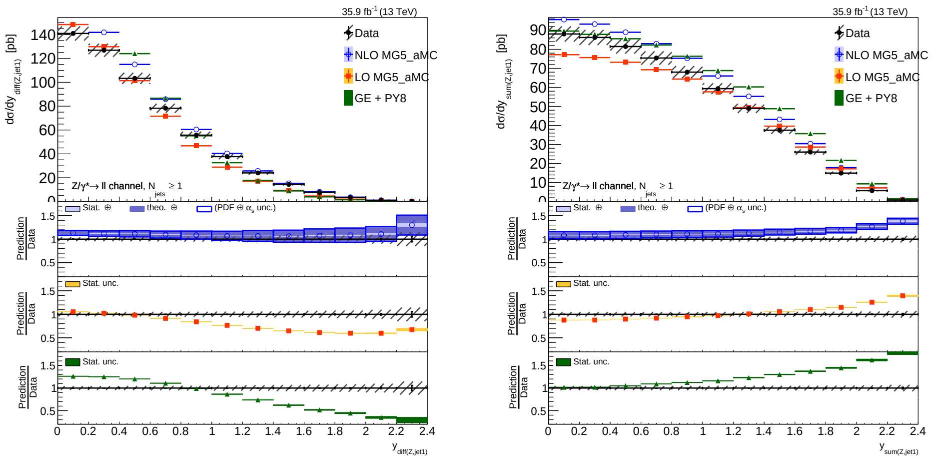

Figure 14: The measured differential cross section as a function of the Z boson and leading jet rapidity difference(left) and sum(right) with at least one jet. For data the black bars show the statstical uncertainty and the hashed area shows the total uncertainty. The measurement is compared to NLO MG5_AMC, LO MG5_AMC, and GENEVA. The uncertainty for predictions is shown only in the ratio plots with statistical, PDF, and scale uncertainties for the NLO MG5_AMC and statistical only for the GENEVA and LO MG5_AMC predictions.

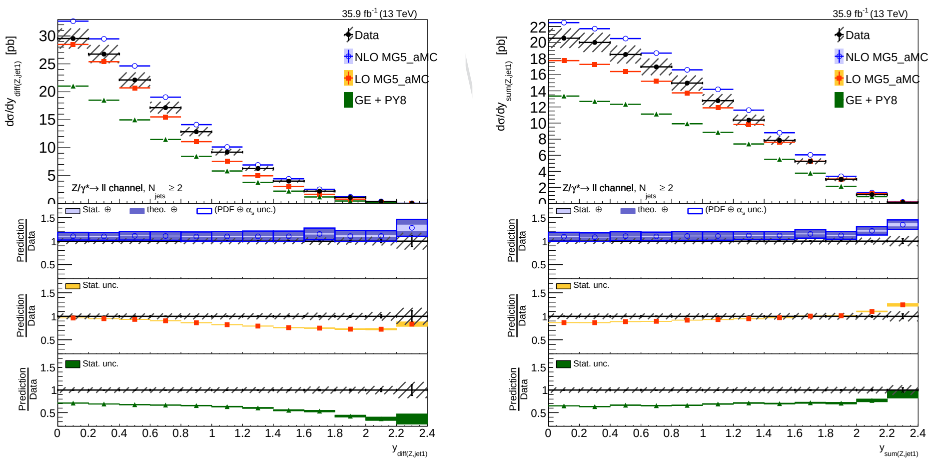

Figure 15: The measured differential cross section as a function of the Z boson and leading jet rapidity difference(left) and sum(right) with at least two jets. For data the black bars show the statstical uncertainty and the hashed area shows the total uncertainty. The measurement is compared to NLO MG5_AMC, LO MG5_AMC, and GENEVA. The uncertainty for predictions is shown only in the ratio plots with statistical, PDF, and scale uncertainties for the NLO MG5_AMC and statistical only for the GENEVA and LO MG5_AMC predictions.

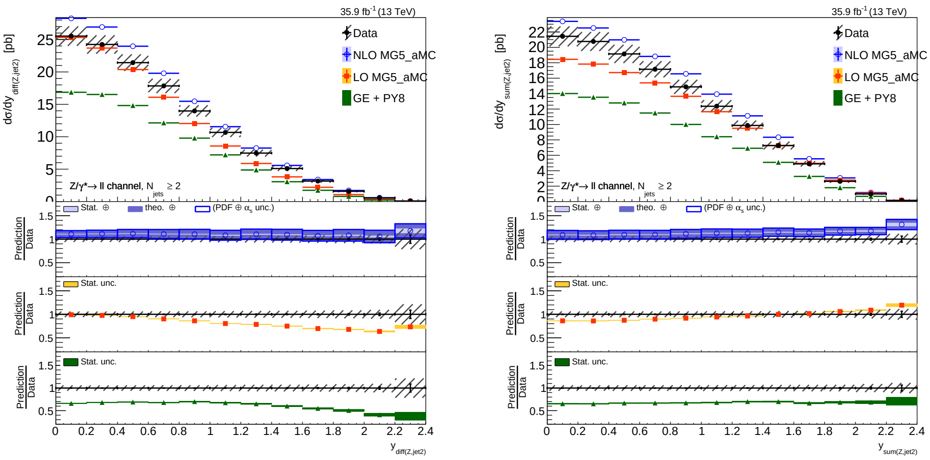

Figure 16: The measured differential cross section as a function of the Z boson and subleading jet rapidity difference(left) and sum(right) with at least two jets. For data the black bars show the statstical uncertainty and the hashed area shows the total uncertainty. The measurement is compared to NLO MG5_AMC, LO MG5_AMC, and GENEVA. The uncertainty for predictions is shown only in the ratio plots with statistical, PDF, and scale uncertainties for the NLO MG5_AMC and statistical only for the GENEVA and LO MG5_AMC predictions.

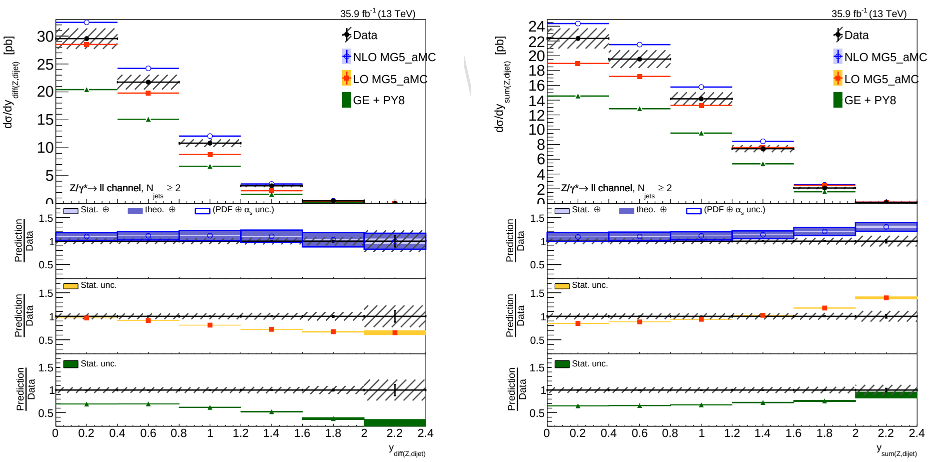

Figure 17: The measured differential cross section as a function of the Z boson and dijet rapidity difference(left) and sum(right) with two jets inclusive. For data the black bars show the statstical uncertainty and the hashed area shows the total uncertainty. The measurement is compared to NLO MG5_AMC, LO MG5_AMC, and GENEVA. The uncertainty for predictions is shown only in the ratio plots with statistical, PDF, and scale uncertainties for the NLO MG5_AMC and statistical only for the GENEVA and LO MG5_AMC predictions.

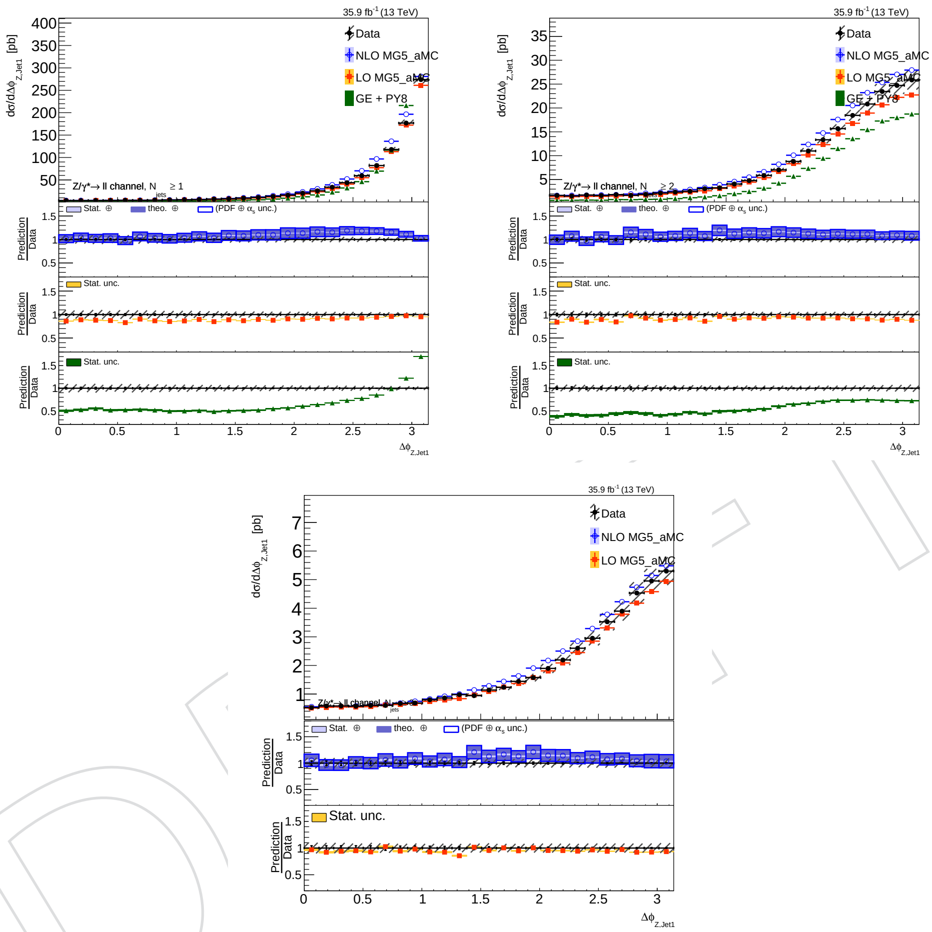

Figure 18: The measured differential cross section as a function of the Z boson and leading jet azimuthal difference with at least one(left), two(middle), and three(right) jets. For data the black bars show the statstical uncertainty and the hashed area shows the total uncertainty. The measurement is compared to NLO MG5_AMC and LO MG5_AMC. The measurements with at least one and two jets is also compared to GENEVA. The uncertainty for predictions is shown only in the ratio plots with statistical, PDF, and scale uncertainties for the NLO MG5_AMC and statistical only for the GENEVA and LO MG5_AMC predictions.

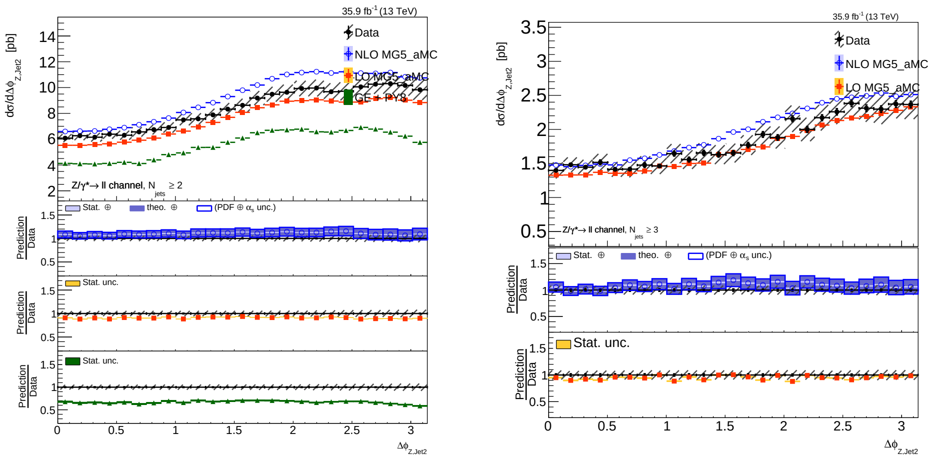

Figure 19: The measured differential cross section as a function of the Z boson and subleading jet azimuthal difference with at least two(left) and three(right) jets. For data the black bars show the statstical uncertainty and the hashed area shows the total uncertainty. The measurement is compared to NLO MG5_AMC and LO MG5_AMC. The measurement with at least two jets is also compared to GENEVA. The uncertainty for predictions is shown only in the ratio plots with statistical, PDF, and scale uncertainties for the NLO MG5_AMC and statistical only for the GENEVA and LO MG5_AMC predictions.

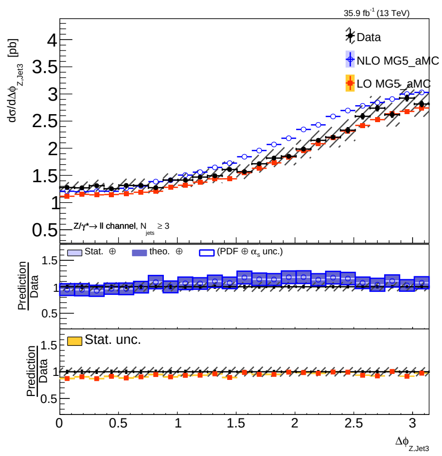

Figure 20: The measured differential cross section as a function of the Z boson and third jet azimuthal difference with at least three jets. For data the black bars show the statstical uncertainty and the hashed area shows the total uncertainty. The measurement is compared to NLO MG5_AMC and LO MG5_AMC. The uncertainty for predictions is shown only in the ratio plots with statistical, PDF, and scale uncertainties for the NLO MG5_AMC and statistical only for the LO MG5_AMC predictions.

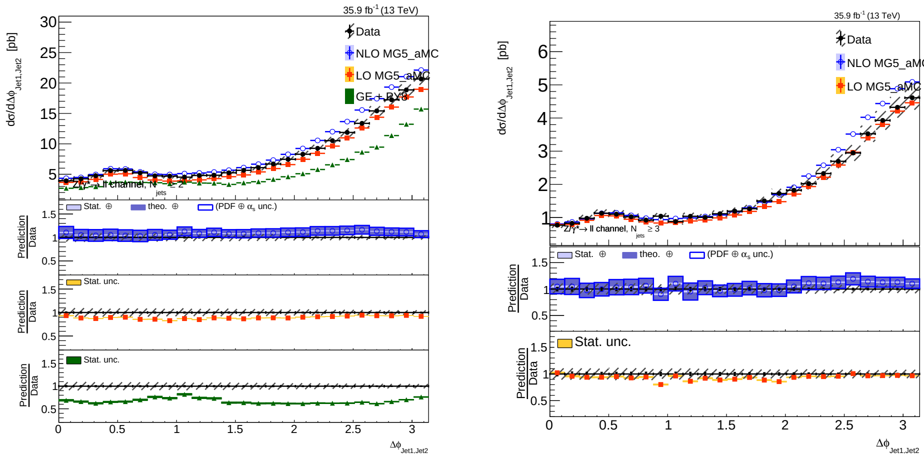

Figure 21: The measured differential cross section as a function of the leading and subleading jet azimuthal difference with at least two(left) and three(right) jets. For data the black bars show the statstical uncertainty and the hashed area shows the total uncertainty. The measurement is compared to NLO MG5_AMC and LO MG5_AMC. The measurement with at least two jets is also compared to GENEVA. The uncertainty for predictions is shown only in the ratio plots with statistical, PDF, and scale uncertainties for the NLO MG5_AMC and statistical only for the GENEVA and LO MG5_AMC predictions.

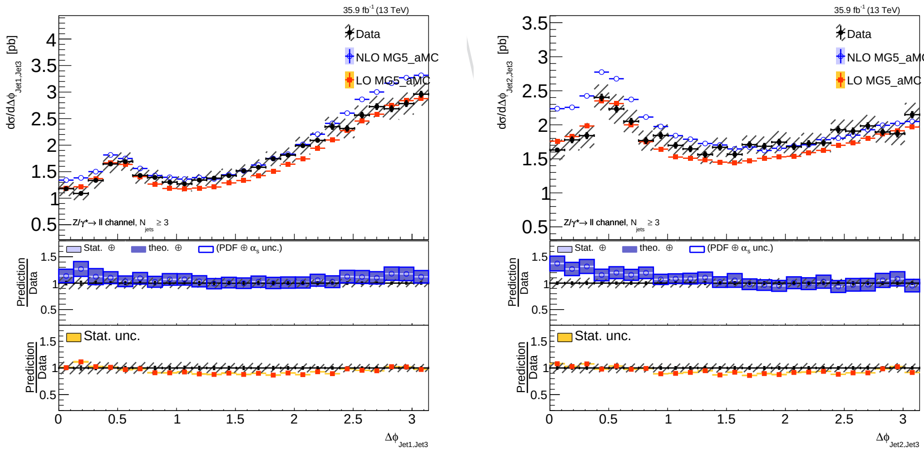

Figure 22: The measured differential cross section as a function of the leading and third jet azimuthal difference(left) and subleading and third jet azimuthal difference(right) with at least three jets. For data the black bars show the statstical uncertainty and the hashed area shows the total uncertainty. The measurement is compared to NLO MG5_AMC and LO MG5_AMC. The uncertainty for predictions is shown only in the ratio plots with statistical, PDF, and scale uncertainties for the NLO MG5_AMC and statistical only for the LO MG5_AMC predictions.

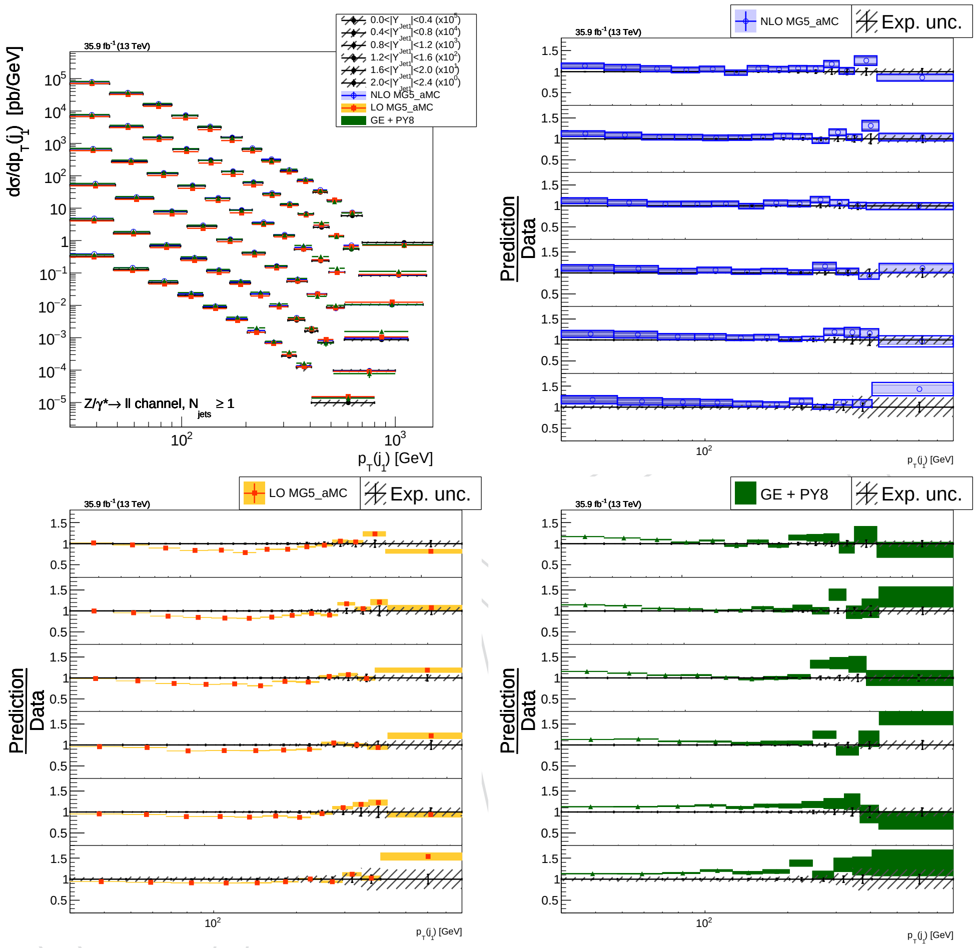

Figure 23: Double differential cross section as a function of leading jet p_T and rapidity with at least one jet (upper left). For data the black bars show the statstical uncertainty and the hashed area shows the total uncertainty. The measurement is compared to NLO MG5_AMC, LO MG5_AMC, and GENEVA and the ratios are shown in the upper right, lower left, and lower right plots, respectively. The uncertainty for predictions is shown only in the ratio plots with statistical, PDF, and scale uncertainties for the NLO MG5_AMC and statistical only for the GENEVA and LO MG5_AMC predictions.

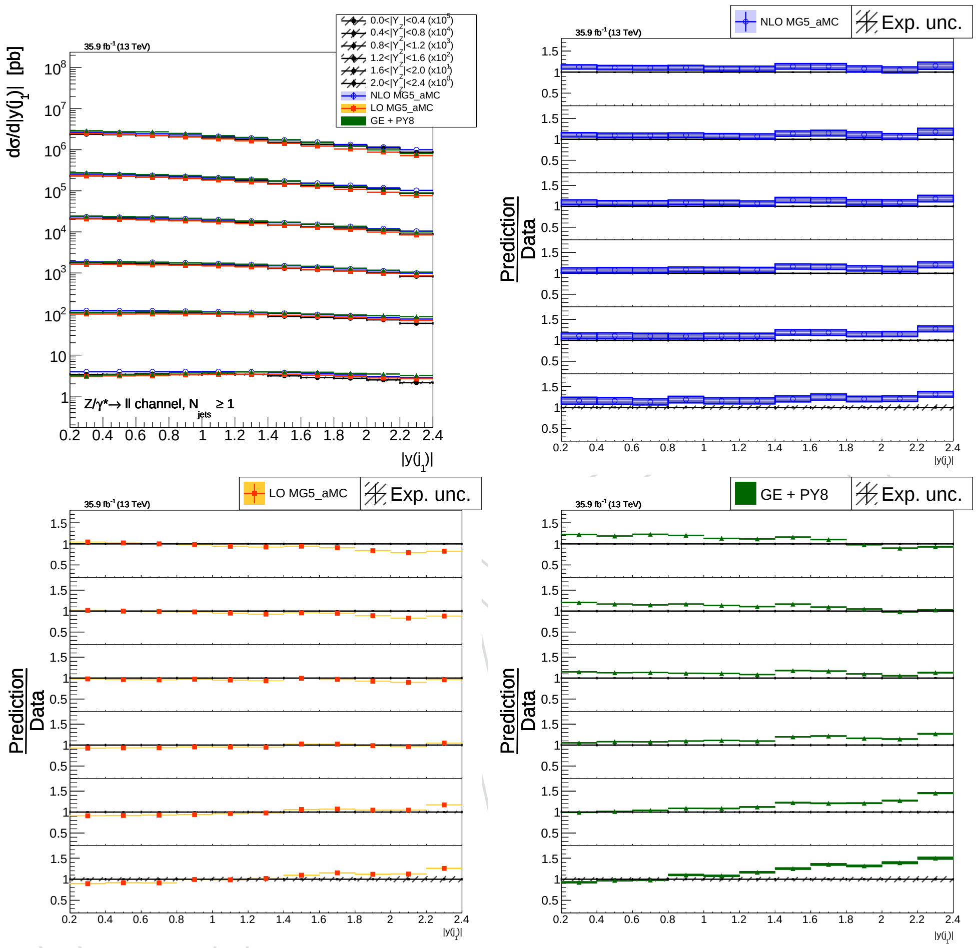

Figure 24: Double differential cross section as a function of leading jet and Z boson rapidity with at least one jet. For data the black bars show the statstical uncertainty and the hashed area shows the total uncertainty. The measurement is compared to NLO MG5_AMC, LO MG5_AMC, and GENEVA and the ratios are shown in the upper right, lower left, and lower right plots, respectively. The uncertainty for predictions is shown only in the ratio plots with statistical, PDF, and scale uncertainties for the NLO MG5_AMC and statistical only for the GENEVA and LO MG5_AMC predictions.

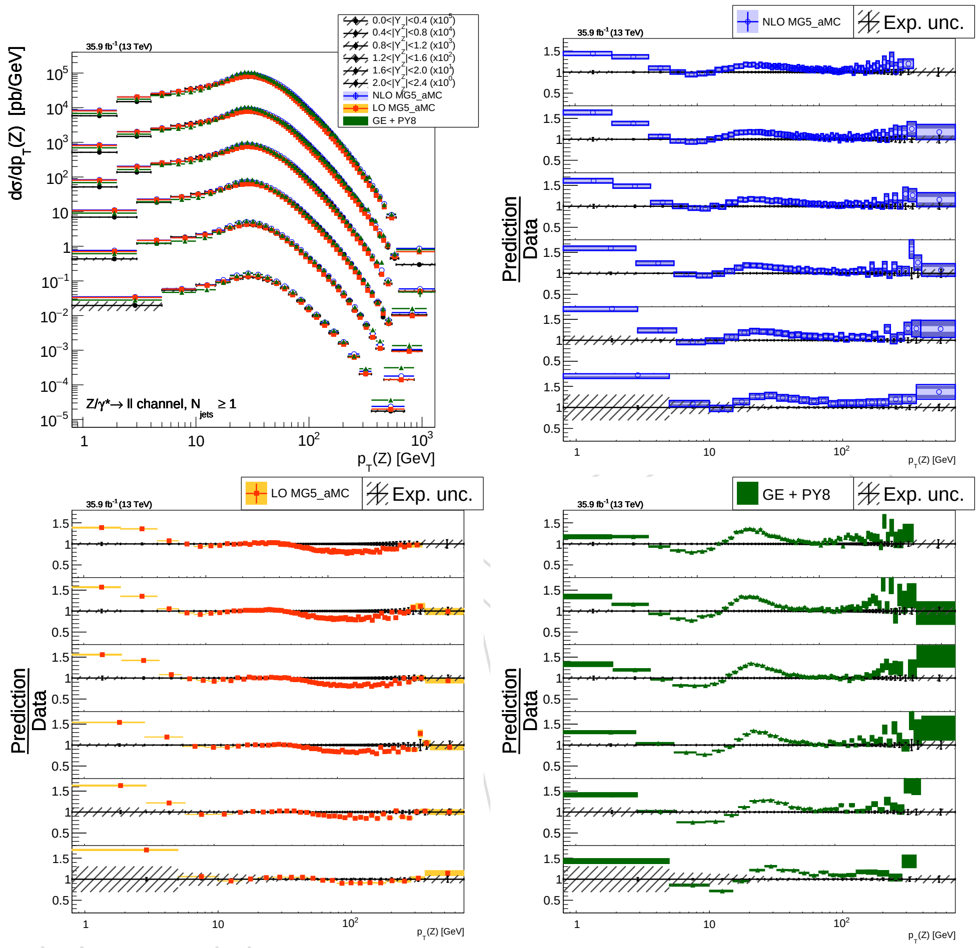

Figure 25: Double differential cross section as a function of Z boson p_T and rapidity with at least one jet. For data the black bars show the statstical uncertainty and the hashed area shows the total uncertainty. The measurement is compared to NLO MG5_AMC, LO MG5_AMC, and GENEVA and the ratios are shown in the upper right, lower left, and lower right plots, respectively. The uncertainty for predictions is shown only in the ratio plots with statistical, PDF, and scale uncertainties for the NLO MG5_AMC and statistical only for the GENEVA and LO MG5_AMC predictions.

Table 1: Differential cross section in 1st jet $|\eta|$ ($N_{\text{jets}} \geq 1$) and break down of the systematic uncertainties for the combination of both decay channels.

$\|y(j_1)\|$	$\frac{d\sigma}{d\|y(j_1)\|}$ [pb]	Tot[%]	stat [%]	JES [%]	JER [%]	Eff [%]	Lumi [%]	XSec [%]	PU [%]	LES+LER [%]	Unf stat [%]
0 − 0.2	67.9	4.3	0.18	1.4	3.0	0.024	0.024	0.037	0.47	0.96	0.13
0.2 − 0.4	68.2	4.3	0.18	1.4	2.9	0.010	0.0099	0.033	0.44	0.98	0.13
0.4 − 0.6	67.2	4.3	0.18	1.4	2.9	0.022	0.021	0.072	0.46	0.97	0.13
0.6 − 0.8	64.9	4.4	0.18	1.4	3.1	0.0049	0.0038	0.11	0.44	0.99	0.14
0.8 − 1	61.6	4.3	0.19	1.4	2.9	0.041	0.041	0.12	0.42	1.0	0.14
1 − 1.2	57.9	5.1	0.19	1.5	4.0	0.017	0.016	0.26	0.42	1.2	0.15
1.2 − 1.4	53.8	5.3	0.20	1.6	4.2	0.025	0.026	0.23	0.63	1.2	0.16
1.4 − 1.6	46.6	5.4	0.23	1.6	4.2	0.0086	0.0080	0.17	0.97	1.1	0.18
1.6 − 1.8	41.6	5.1	0.25	1.6	3.7	0.048	0.048	0.51	1.4	1.2	0.20
1.8 − 2	37.7	5.6	0.26	1.7	4.2	0.015	0.011	0.90	1.7	1.2	0.22
2 − 2.2	33.5	6.8	0.28	1.9	5.4	0.030	0.028	1.2	1.7	1.5	0.25
2.2 − 2.4	26.6	8.7	0.35	2.3	7.2	0.035	0.031	1.6	2.1	2.0	0.33

Table 2: Differential cross section in 1st jet p_T ($N_{\text{jets}} \geq 1$) and break down of the systematic uncertainties for the combination of both decay channels.

$p_T(j_1)$ [GeV]	$\frac{d\sigma}{dp_T(j_1)}$ $[\frac{\text{pb}}{\text{GeV}}]$	Tot[%]	stat [%]	JES [%]	JER [%]	Eff [%]	Lumi [%]	XSec [%]	PU [%]	LES+LER [%]	Unf stat [%]
30 − 47	3.45	4.1	0.13	1.2	2.8	0.015	0.0099	0.24	0.65	0.99	0.13
47 − 69	1.51	3.9	0.17	1.3	2.4	0.021	0.022	0.059	0.51	0.90	0.16
69 − 96	0.640	4.3	0.23	1.4	3.0	0.022	0.022	0.19	0.32	0.97	0.21
96 − 128	0.266	4.3	0.33	1.4	2.9	0.020	0.019	0.084	0.43	0.90	0.30
128 − 166	0.113	4.0	0.48	1.4	2.6	0.021	0.021	0.14	0.31	0.69	0.43
166 − 210	0.0492	4.6	0.67	1.5	3.2	0.031	0.031	0.17	0.29	1.1	0.60
210 − 261	0.0203	4.4	0.98	1.4	2.7	0.076	0.077	0.12	0.30	0.94	0.88
261 − 319	0.00903	4.9	1.3	1.6	3.2	0.066	0.066	0.19	0.56	0.94	1.2
319 − 386	0.00376	5.2	1.9	1.6	2.9	0.086	0.087	0.36	0.12	1.4	1.7
386 − 460	0.00167	6.5	2.8	1.9	4.1	0.13	0.13	0.15	0.53	1.3	2.4
460 − 544	0.000689	7.7	3.9	2.5	1.8	0.31	0.32	0.22	1.2	3.4	3.6
544 − 638	0.000313	11.	5.5	2.4	6.7	0.25	0.27	0.11	0.69	2.8	5.2
638 − 751	0.000134	12.	7.5	3.1	2.2	0.18	0.22	0.48	1.0	2.4	7.6
751 − 870	5.81e-05	19.	11.	1.8	7.3	0.41	0.41	0.75	2.0	1.2	12.
870 − 1500	1.16e-05	17.	11.	1.6	4.9	0.36	0.36	0.77	1.6	0.90	11.

Table 3: Differential cross section in exclusive jet multiplicity and break down of the systematic uncertainties for the combination of both decay channels.

N_{jets}	$\frac{d\sigma}{dN_{\text{jets}}}$ [pb]	Tot[%]	stat [%]	JES [%]	JER [%]	Eff [%]	Lumi [%]	XSec [%]	PU [%]	LES+LER [%]	Unf stat [%]
= 0	615.	2.9	0.022	0.87	0.78	0.021	0.021	0.087	0.11	0.59	0.013
= 1	96.8	4.9	0.072	1.5	3.7	0.019	0.018	0.34	0.67	1.1	0.063
= 2	22.1	5.2	0.18	1.5	4.0	0.013	0.013	0.22	0.85	1.1	0.16
= 3	4.63	6.5	0.47	1.8	5.4	0.022	0.024	0.26	1.0	1.4	0.43
= 4	1.10	8.0	1.1	2.2	6.6	0.13	0.13	0.42	1.9	1.9	1.1
= 5	0.235	9.1	3.0	2.6	6.3	0.12	0.22	1.2	0.62	2.7	3.1
= 6	0.0645	15.	6.5	1.3	9.7	0.18	1.2	2.1	1.4	1.0	7.5
= 7	0.0135	35.	17.	6.2	17.	0.94	3.5	3.7	11.	2.6	22.
= 8	0.00288	41.	25.	6.4	14.	0.99	1.4	2.7	2.4	2.6	29.

Table 4: Differential cross section in p_T^Z and break down of the systematic uncertainties for the combination of both decay channels.

$p_{\mathrm{T}}(Z)$ [GeV]	$\frac{d\sigma}{dp_{\mathrm{T}}(Z)}$ [$\frac{\mathrm{pb}}{\mathrm{GeV}}$]	Tot[%]	stat [%]	JES [%]	JER [%]	Eff [%]	Lumi [%]	XSec [%]	PU [%]	LES+LER [%]	Unf stat [%]
0.8 − 2	0.0789	24.	3.7	4.4	22.	0.40	0.26	4.2	0.97	3.4	2.1
2 − 4	0.201	23.	2.4	5.6	22.	0.34	0.31	2.9	1.7	5.2	1.5
4 − 6	0.341	16.	1.6	3.7	15.	0.20	0.27	2.2	0.37	3.4	1.1
6 − 8	0.442	13.	1.3	3.0	12.	0.28	0.31	1.9	0.25	2.9	1.0
8 − 10	0.525	13.	1.1	3.2	11.	0.49	0.54	1.5	0.39	2.5	0.97
10 − 12	0.630	12.	1.0	2.9	11.	0.18	0.18	1.6	0.76	2.6	0.89
12 − 14	0.688	12.	0.99	3.0	11.	0.17	0.18	1.5	0.89	2.6	0.89
14 − 16	0.791	12.	0.89	2.9	11.	0.12	0.13	1.3	1.1	2.3	0.81
16 − 19	0.873	13.	0.62	3.0	11.	0.10	0.12	1.6	1.1	2.5	0.56
19 − 22	1.00	13.	0.58	3.2	12.	0.21	0.19	1.5	1.3	2.5	0.52
22 − 25	1.15	13.	0.56	3.4	12.	0.070	0.19	1.4	1.4	2.7	0.48
25 − 28	1.33	12.	0.51	3.0	11.	0.17	0.17	1.1	1.4	2.7	0.44
28 − 31	1.56	10.	0.45	2.7	9.4	0.10	0.12	0.78	1.3	2.3	0.40
31 − 34	1.77	8.4	0.42	2.2	7.3	0.017	0.018	0.45	1.3	1.9	0.37
34 − 37	1.95	7.0	0.39	1.9	5.9	0.16	0.16	0.37	1.1	1.6	0.35
37 − 40	2.03	5.9	0.37	1.7	4.7	0.014	0.021	0.18	1.1	1.3	0.34
40 − 43	2.03	5.0	0.38	1.5	3.7	0.079	0.078	0.11	0.99	1.1	0.35
43 − 46	1.99	4.6	0.38	1.5	3.2	0.035	0.039	0.10	0.86	1.2	0.35
46 − 49	1.90	4.1	0.39	1.4	2.5	0.042	0.043	0.030	0.95	0.96	0.36
49 − 53	1.77	3.7	0.32	1.3	2.1	0.0067	0.0075	0.027	0.77	0.83	0.29
53 − 57	1.61	3.5	0.34	1.3	1.6	0.11	0.11	0.030	0.77	1.0	0.31
57 − 61	1.45	3.4	0.36	1.3	1.4	0.0097	0.011	0.014	0.64	0.87	0.33
61 − 65	1.30	3.2	0.39	1.2	0.99	0.16	0.16	0.0055	0.60	0.93	0.35
65 − 69	1.14	3.2	0.42	1.2	0.86	0.028	0.028	0.023	0.53	0.86	0.38
69 − 73	1.00	3.1	0.45	1.2	0.72	0.085	0.086	0.013	0.56	0.76	0.41
73 − 78	0.860	3.1	0.41	1.2	0.61	0.11	0.12	0.013	0.51	0.91	0.37
78 − 83	0.731	3.0	0.45	1.2	0.45	0.096	0.095	0.032	0.43	0.58	0.40
83 − 88	0.611	3.1	0.50	1.2	0.37	0.13	0.13	0.0032	0.42	0.75	0.44
88 − 93	0.514	3.1	0.56	1.2	0.34	0.14	0.14	0.020	0.30	1.0	0.50
93 − 99	0.439	3.1	0.52	1.2	0.26	0.22	0.22	0.00077	0.49	0.67	0.45
99 − 105	0.361	3.1	0.59	1.3	0.25	0.0079	0.017	0.016	0.50	0.98	0.51
105 − 111	0.301	3.1	0.66	1.3	0.24	0.24	0.24	0.024	0.22	0.75	0.58
111 − 118	0.247	3.1	0.66	1.3	0.16	0.15	0.15	0.025	0.42	0.62	0.58
118 − 125	0.212	3.4	0.72	1.3	0.14	0.14	0.14	0.0083	0.39	1.6	0.63
125 − 133	0.172	3.1	0.74	1.3	0.12	0.27	0.27	0.035	0.16	0.50	0.65
133 − 141	0.141	3.2	0.84	1.3	0.12	0.12	0.12	0.020	0.14	0.90	0.74
141 − 150	0.115	3.3	0.86	1.3	0.11	0.43	0.43	0.017	0.38	0.72	0.75
150 − 160	0.0882	3.2	0.93	1.3	0.043	0.013	0.014	0.038	0.47	0.50	0.80
160 − 171	0.0718	3.4	0.97	1.4	0.081	0.31	0.31	0.0081	0.044	1.3	0.83
171 − 183	0.0549	3.6	1.1	1.4	0.080	0.27	0.27	0.0067	0.63	1.4	0.92
183 − 197	0.0412	3.3	1.1	1.3	0.053	0.22	0.22	0.039	0.053	0.57	0.96
197 − 212	0.0318	3.6	1.3	1.4	0.049	0.18	0.18	0.022	0.23	1.4	1.1
212 − 228	0.0229	3.6	1.4	1.4	0.025	0.22	0.22	0.039	0.40	0.56	1.2
228 − 246	0.0172	3.7	1.6	1.4	0.0023	0.44	0.44	0.082	0.13	0.54	1.3
246 − 266	0.0119	3.9	1.8	1.4	0.013	0.18	0.18	0.039	0.17	0.83	1.5
266 − 289	0.00839	4.0	1.9	1.5	0.0083	0.30	0.30	0.019	0.37	0.78	1.6
289 − 314	0.00592	4.6	2.2	1.6	0.040	0.46	0.46	0.0082	0.29	1.8	1.9
314 − 344	0.00369	4.6	2.5	1.6	0.063	0.27	0.27	0.040	0.43	0.84	2.1
344 − 377	0.00244	5.1	2.9	1.7	0.086	0.57	0.57	0.050	0.42	0.96	2.4
377 − 418	0.00149	5.6	3.2	1.8	0.022	0.53	0.54	0.024	0.15	2.0	2.6
418 − 460	0.000845	6.8	4.3	2.1	0.10	0.025	0.12	0.13	1.0	1.8	3.3
460 − 511	0.000490	7.4	4.5	2.6	0.018	1.2	1.2	0.0071	0.49	2.3	3.6
511 − 567	0.000255	8.9	5.9	2.9	0.027	0.039	0.091	0.0093	1.3	2.6	4.5
567 − 1300	3.07e-05	6.3	4.2	1.9	0.057	1.1	1.2	0.011	0.38	1.6	2.6

Table 5: Differential cross section in $|y_Z|$ ($N_{\text{jets}} \geq 1$) and break down of the systematic uncertainties for the combination of both decay channels.

$\lvert y_Z \rvert$	$\frac{d\sigma}{d\lvert y_Z \rvert}$ [pb]	Tot[%]	stat [%]	JES [%]	JER [%]	Eff [%]	Lumi [%]	XSec [%]	PU [%]	LES+LER [%]	Unf stat [%]
0 − 0.2	70.3	5.0	0.15	1.6	3.7	0.035	0.034	0.31	0.74	1.3	0.12
0.2 − 0.4	69.9	4.9	0.15	1.6	3.6	0.018	0.014	0.28	0.75	1.2	0.12
0.4 − 0.6	69.4	4.9	0.15	1.6	3.6	0.036	0.035	0.29	0.68	1.2	0.12
0.6 − 0.8	68.6	4.9	0.16	1.6	3.6	0.031	0.030	0.29	0.70	1.2	0.12
0.8 − 1	67.2	4.9	0.16	1.5	3.6	0.0071	0.0073	0.29	0.72	1.1	0.12
1 − 1.2	64.6	4.9	0.17	1.4	3.7	0.023	0.024	0.27	0.72	1.0	0.12
1.2 − 1.4	60.3	4.9	0.18	1.3	3.7	0.025	0.025	0.31	0.72	0.94	0.13
1.4 − 1.6	53.3	4.8	0.20	1.3	3.7	0.0043	0.0042	0.29	0.76	0.91	0.14
1.6 − 1.8	44.2	4.8	0.22	1.2	3.7	0.0045	0.00088	0.26	0.78	0.73	0.16
1.8 − 2	33.1	4.8	0.26	1.2	3.6	0.020	0.020	0.28	0.84	0.82	0.18
2 − 2.2	20.7	4.8	0.32	1.4	3.5	0.015	0.013	0.27	0.98	0.91	0.24
2.2 − 2.4	6.72	5.0	0.59	1.7	3.5	0.014	0.018	0.27	1.1	1.4	0.45

11 Summary

The production of Z bosons decaying into two charged leptons in association with jets is studied in LHC pp collisions at centre-of-mass energy of 13 TeV with the CMS experiment, using data sets corresponding to an integrated luminosity of 35.9 fb^{-1}. Differential cross sections are measured for Z bosons decaying to electrons or muons with $p_{\mathrm{T}} > 25$ GeV and $|\eta| < 2.4$ with at least one jet with $p_{\mathrm{T}} > 30$ GeV and $|\eta| < 2.4$.

The differential cross sections have been measured as functions of the exclusive and inclusive jet multiplicities up to 8, of the transverse momentum of the Z boson, jet kinematic variables including jet transverse momenta, the scalar sum of jet transverse momenta, and the jet rapidity for inclusive jet multiplicities up to five jets.

The results, corrected for all detector effects by means of regularized unfolding, have been compared with three different calculations. Two predictions are particle-level simulations where one uses multileg NLO predictions using the FxFx merging scheme and the other uses multileg LO predictions and the MLM matching scheme. The third calculation is the GENEVA MC program, where an NNLO calculation for Drell-Yan production is combined with higher-order resummation.

High precision has been achieved in the CMS measurements of cross sections and their ratios using the latest experimental methods and larger datasets than in previous CMS publications. The larger datasets have extended the kinematic range of cross section measurements to higher values of p_{T} and mass, as well as opening up the possibility to investigate rare processes not yet observed. The measurements presented in this paper provide a detailed description of the topological structure of $\mathrm{Z}(\rightarrow \ell^+\ell^-) +$ jets production that is complementary to existing measurements of rates and associated jet multiplicities.

In summary the measured cross sections are generally described by the predictions within the experimental and theoretical uncertainties. The predictions describe the jet multiplicity within the uncertainties, with increasing deviations observed for jet multiplicities beyond three. A general agreement is observed for the distribution of the jet variable considered. However, some deviations from data are seen.

The results indicate that multiparton NLO calculations and the associated uncertainty should be used for the estimation of the $\mathrm{Z}(\rightarrow \ell^+\ell^-) +$ jets contributions to measurements and searches at the LHC.

Acknowledgments

We congratulate our colleagues in the CERN accelerator departments for the excellent performance of the LHC and thank the technical and administrative staffs at CERN and at other CMS institutes for their contributions to the success of the CMS effort. In addition, we gratefully acknowledge the computing centers and personnel of the Worldwide LHC Computing Grid for delivering so effectively the computing infrastructure essential to our analyses. Finally, we acknowledge the enduring support for the construction and operation of the LHC and the CMS detector provided by the following funding agencies: the Austrian Federal Ministry of Education, Science and Research and the Austrian Science Fund; the Belgian Fonds de la Recherche Scientifique, and Fonds voor Wetenschappelijk Onderzoek; the Brazilian Funding Agencies (CNPq, CAPES, FAPERJ, FAPERGS, and FAPESP); the Bulgarian Ministry of Education and Science; CERN; the Chinese Academy of Sciences, Ministry of Science and Technology, and National Natural Science Foundation of China; the Colombian Funding Agency

(COLCIENCIAS); the Croatian Ministry of Science, Education and Sport, and the Croatian Science Foundation; the Research Promotion Foundation, Cyprus; the Secretariat for Higher Education, Science, Technology and Innovation, Ecuador; the Ministry of Education and Research, Estonian Research Council via IUT23-4, IUT23-6 and PRG445 and European Regional Development Fund, Estonia; the Academy of Finland, Finnish Ministry of Education and Culture, and Helsinki Institute of Physics; the Institut National de Physique Nucléaire et de Physique des Particules / CNRS, and Commissariat à l'Énergie Atomique et aux Énergies Alternatives / CEA, France; the Bundesministerium für Bildung und Forschung, Deutsche Forschungsgemeinschaft, and Helmholtz-Gemeinschaft Deutscher Forschungszentren, Germany; the General Secretariat for Research and Technology, Greece; the National Research, Development and Innovation Fund, Hungary; the Department of Atomic Energy and the Department of Science and Technology, India; the Institute for Studies in Theoretical Physics and Mathematics, Iran; the Science Foundation, Ireland; the Istituto Nazionale di Fisica Nucleare, Italy; the Ministry of Science, ICT and Future Planning, and National Research Foundation (NRF), Republic of Korea; the Ministry of Education and Science of the Republic of Latvia; the Lithuanian Academy of Sciences; the Ministry of Education, and University of Malaya (Malaysia); the Ministry of Science of Montenegro; the Mexican Funding Agencies (BUAP, CINVESTAV, CONACYT, LNS, SEP, and UASLP-FAI); the Ministry of Business, Innovation and Employment, New Zealand; the Pakistan Atomic Energy Commission; the Ministry of Science and Higher Education and the National Science Centre, Poland; the Fundação para a Ciência e a Tecnologia, Portugal; JINR, Dubna; the Ministry of Education and Science of the Russian Federation, the Federal Agency of Atomic Energy of the Russian Federation, Russian Academy of Sciences, the Russian Foundation for Basic Research, and the National Research Center "Kurchatov Institute"; the Ministry of Education, Science and Technological Development of Serbia; the Secretaría de Estado de Investigación, Desarrollo e Innovación, Programa Consolider-Ingenio 2010, Plan Estatal de Investigación Científica y Técnica y de Innovación 2017–2020, research project IDI-2018-000174 del Principado de Asturias, and Fondo Europeo de Desarrollo Regional, Spain; the Ministry of Science, Technology and Research, Sri Lanka; the Swiss Funding Agencies (ETH Board, ETH Zurich, PSI, SNF, UniZH, Canton Zurich, and SER); the Ministry of Science and Technology, Taipei; the Thailand Center of Excellence in Physics, the Institute for the Promotion of Teaching Science and Technology of Thailand, Special Task Force for Activating Research and the National Science and Technology Development Agency of Thailand; the Scientific and Technical Research Council of Turkey, and Turkish Atomic Energy Authority; the National Academy of Sciences of Ukraine, and State Fund for Fundamental Researches, Ukraine; the Science and Technology Facilities Council, UK; the US Department of Energy, and the US National Science Foundation.

Individuals have received support from the Marie-Curie programme and the European Research Council and Horizon 2020 Grant, contract Nos. 675440, 752730, and 765710 (European Union); the Leventis Foundation; the A.P. Sloan Foundation; the Alexander von Humboldt Foundation; the Belgian Federal Science Policy Office; the Fonds pour la Formation à la Recherche dans l'Industrie et dans l'Agriculture (FRIA-Belgium); the Agentschap voor Innovatie door Wetenschap en Technologie (IWT-Belgium); the F.R.S.-FNRS and FWO (Belgium) under the "Excellence of Science – EOS" – be.h project n. 30820817; the Beijing Municipal Science & Technology Commission, No. Z181100004218003; the Ministry of Education, Youth and Sports (MEYS) of the Czech Republic; the Lendület ("Momentum") Programme and the János Bolyai Research Scholarship of the Hungarian Academy of Sciences, the New National Excellence Program ÚNKP, the NKFIA research grants 123842, 123959, 124845, 124850, 125105, 128713, 128786, and 129058 (Hungary); the Council of Scientific and Industrial Research, India; the HOMING PLUS programme of the Foundation for Polish Science, cofinanced from European Union, Regional Development Fund, the Mobility Plus programme of the Ministry of Science and Higher Education, the National Science Center (Poland), contracts Harmonia 2014/14/M/ST2/00428, Opus 2014/13/B/ST2/02543, 2014/15/B/ST2/03998, and 2015/19/B/ST2/02861, Sonata-bis 2012/07/E/ST2/01406; the National Priorities Research Program by Qatar National Research Fund; the Ministry of Science and Education, grant no. 3.2989.2017 (Russia); the Programa de Excelencia María de Maeztu, and the Programa Severo Ochoa del Principado de Asturias; the Thalis and Aristeia programmes cofinanced by EU-ESF, and the Greek NSRF; the Rachadapisek Sompot Fund for Postdoctoral Fellowship, Chulalongkorn University, and the Chulalongkorn Academic into Its 2nd Century Project Advancement Project (Thailand); the Welch Foundation, contract C-1845; and the Weston Havens Foundation (USA).

References

[1] S. D. Drell and T.-M. Yan, "Massive Lepton Pair Production in Hadron-Hadron Collisions at High-Energies", *Phys. Rev. Lett.* **25** (1970) 316–320, doi:10.1103/PhysRevLett.25.316,10.1103/PhysRevLett.25.902.2. [Erratum: Phys. Rev. Lett.25,902(1970)].

[2] R. Hamberg, W. L. van Neerven, and T. Matsuura, "A complete calculation of the order $\alpha - s^2$ correction to the Drell-Yan K factor", *Nucl. Phys.* **B359** (1991) 343–405, doi:10.1016/S0550-3213(02)00814-3,10.1016/0550-3213(91)90064-5. [Erratum: Nucl. Phys.B644,403(2002)].

[3] S. Catani and M. Grazzini, "An NNLO subtraction formalism in hadron collisions and its application to Higgs boson production at the LHC", *Phys. Rev. Lett.* **98** (2007) 222002, doi:10.1103/PhysRevLett.98.222002, arXiv:hep-ph/0703012.

[4] K. Melnikov and F. Petriello, "Electroweak gauge boson production at hadron colliders through O(alpha(s)**2)", *Phys. Rev.* **D74** (2006) 114017, doi:10.1103/PhysRevD.74.114017, arXiv:hep-ph/0609070.

[5] ATLAS Collaboration, "Measurement of the production cross section of jets in association with a Z boson in pp collisions at $\sqrt{s}$ = 7 TeV with the ATLAS detector", *JHEP* **07** (2013) 032, doi:10.1007/JHEP07(2013)032, arXiv:1304.7098.

[6] ATLAS Collaboration, "Measurement of the production cross section for Z/gamma* in association with jets in pp collisions at $\sqrt{s} = 7$ TeV with the ATLAS detector", *Phys. Rev.* **D85** (2012) 032009, doi:10.1103/PhysRevD.85.032009, arXiv:1111.2690.

[7] CMS Collaboration, "Jet Production Rates in Association with W and Z Bosons in pp Collisions at $\sqrt{s} = 7$ TeV", *JHEP* **01** (2012) 010, doi:10.1007/JHEP01(2012)010, arXiv:1110.3226.

[8] CMS Collaboration, "Measurements of jet multiplicity and differential production cross sections of $Z+$ jets events in proton-proton collisions at $\sqrt{s} = 7$ TeV", *Phys. Rev.* **D91** (2015), no. 5, 052008, doi:10.1103/PhysRevD.91.052008, arXiv:1408.3104.

[9] CMS Collaboration, "Comparison of the Z/γ^* + jets to γ + jets cross sections in pp collisions at $\sqrt{s} = 8$ TeV", *JHEP* **10** (2015) 128, doi:10.1007/JHEP04(2016)010,10.1007/JHEP10(2015)128, arXiv:1505.06520. [Erratum: JHEP04,010(2016)].

[10] CMS Collaboration, "Measurements of differential production cross sections for a Z boson in association with jets in pp collisions at $\sqrt{s} = 8$ TeV", *JHEP* **04** (2017) 022, doi:10.1007/JHEP04(2017)022, arXiv:1611.03844.

[11] LHCb Collaboration, "Measurement of forward W and Z boson production in association with jets in proton-proton collisions at $\sqrt{s} = 8$ TeV", *JHEP* **05** (2016) 131, doi:10.1007/JHEP05(2016)131, arXiv:1605.00951.

[12] CMS Collaboration, "Measurement of differential cross sections for Z boson production in association with jets in proton-proton collisions at $\sqrt{s} = 13$ TeV", *Eur. Phys. J.* **C78** (2018), no. 11, 965, doi:10.1140/epjc/s10052-018-6373-0, arXiv:1804.05252.

[13] ATLAS Collaboration, "Measurements of the production cross section of a Z boson in association with jets in pp collisions at $\sqrt{s} = 13$ TeV with the ATLAS detector", *Eur. Phys. J.* **C77** (2017), no. 6, 361, doi:10.1140/epjc/s10052-017-4900-z, arXiv:1702.05725.

[14] CDF Collaboration, "Measurement of inclusive jet cross-sections in $Z/\gamma^* \to e^+e^-$ + jets production in $p\bar{p}$ collisions at $\sqrt{s}$ = 1.96-TeV", *Phys. Rev. Lett.* **100** (2008) 102001, doi:10.1103/PhysRevLett.100.102001, arXiv:0711.3717.

[15] D0 Collaboration, "Measurement of differential Z/γ^* + jet + X cross sections in $p\bar{p}$ collisions at $\sqrt{s}$ = 1.96-TeV", *Phys. Lett.* **B669** (2008) 278–286, doi:10.1016/j.physletb.2008.09.060, arXiv:0808.1296.

[16] CMS Collaboration, "Description and performance of track and primary-vertex reconstruction with the CMS tracker", *JINST* **9** (2014) P10009, doi:10.1088/1748-0221/9/10/P10009, arXiv:1405.6569.

[17] CMS Collaboration, "Performance of photon reconstruction and identification with the CMS detector in proton-proton collisions at $\sqrt{s} = 8$ TeV", *JINST* **10** (2015) P08010, doi:10.1088/1748-0221/10/08/P08010, arXiv:1502.02702.

[18] CMS Collaboration, "Performance of CMS Muon Reconstruction in pp Collision Events at $\sqrt{s} = 7$ TeV", *JINST* **7** (2012) P10002, doi:10.1088/1748-0221/7/10/P10002, arXiv:1206.4071.

[19] CMS Collaboration, "The CMS trigger system", *JINST* **12** (2017), no. 01, P01020, doi:10.1088/1748-0221/12/01/P01020, arXiv:1609.02366.

[20] CMS Collaboration, "The CMS experiment at the CERN LHC", *JINST* **3** (2008) S08004, doi:10.1088/1748-0221/3/08/S08004.

[21] J. Allison et al., "GEANT4 developments and applications", *IEEE Trans. Nucl. Sci.* **53** (2006) 270, doi:10.1109/TNS.2006.869826.

[22] J. Alwall et al., "Comparative study of various algorithms for the merging of parton showers and matrix elements in hadronic collisions", *Eur. Phys. J.* **C53** (2008) 473–500, doi:10.1140/epjc/s10052-007-0490-5, arXiv:0706.2569.

[23] R. Frederix and S. Frixione, "Merging meets matching in MC@NLO", *Journal of High Energy Physics* **2012** (Dec, 2012) 61, doi:10.1007/JHEP12(2012)061, arXiv:1209.6215.

[24] T. Sjöstrand, S. Mrenna, and P. Skands, "A brief introduction to PYTHIA 8.1", *Computer Physics Communications* **178** (Jun, 2008) 852–867, doi:10.1016/j.cpc.2008.01.036, arXiv:0710.3820.

[25] CMS Collaboration, "Event generator tunes obtained from underlying event and multiparton scattering measurements", *arXiv e-prints* (Dec, 2015) arXiv:1512.00815, arXiv:1512.00815.

[26] J. M. Campbell, R. K. Ellis, and C. Williams, "Vector boson pair production at the LHC", *JHEP* **07** (2011) 018, doi:10.1007/JHEP07(2011)018, arXiv:1105.0020.

[27] P. Nason, "A new method for combining NLO QCD with shower Monte Carlo algorithms", *JHEP* **11** (2004) 040, doi:10.1088/1126-6708/2004/11/040, arXiv:hep-ph/0409146.

[28] S. Frixione, P. Nason, and C. Oleari, "Matching NLO QCD computations with parton shower simulations: the POWHEG method", *JHEP* **11** (2007) 070, doi:10.1088/1126-6708/2007/11/070, arXiv:0709.2092.

[29] S. Alioli, P. Nason, C. Oleari, and E. Re, "A general framework for implementing NLO calculations in shower Monte Carlo programs: the POWHEG BOX", *JHEP* **06** (2010) 043, doi:10.1007/JHEP06(2010)043, arXiv:1002.2581.

[30] S. Frixione, P. Nason, and G. Ridolfi, "A Positive-weight next-to-leading-order Monte Carlo for heavy flavour hadroproduction", *JHEP* **09** (2007) 126, doi:10.1088/1126-6708/2007/09/126, arXiv:0707.3088.

[31] CMS Collaboration, "Particle-flow reconstruction and global event description with the cms detector", *JINST* **12** (2017) P10003, doi:10.1088/1748-0221/12/10/P10003, arXiv:1706.04965.

[32] M. Cacciari, G. P. Salam, and G. Soyez, "The anti-k_t jet clustering algorithm", *JHEP* **04** (2008) 063, doi:10.1088/1126-6708/2008/04/063, arXiv:0802.1189.

[33] M. Cacciari, G. P. Salam, and G. Soyez, "FastJet user manual", *Eur. Phys. J. C* **72** (2012) 1896, doi:10.1140/epjc/s10052-012-1896-2, arXiv:1111.6097.

[34] CMS Collaboration, "Performance of Electron Reconstruction and Selection with the CMS Detector in Proton-Proton Collisions at sqrt(s) = 8 TeV", *JINST* **10** (2015), no. 06, P06005, doi:10.1088/1748-0221/10/06/P06005, arXiv:1502.02701.

[35] M. Cacciari, G. P. Salam, and G. Soyez, "The anti-k$_t$ jet clustering algorithm", *Journal of High Energy Physics* **2008** (Apr, 2008) 063, doi:10.1088/1126-6708/2008/04/063, arXiv:0802.1189.

[36] CMS Collaboration, "Pileup Removal Algorithms",.

[37] CMS Collaboration, "Measurement of the Inclusive W and Z Production Cross Sections in pp Collisions at $\sqrt{s} = 7$ TeV", *JHEP* **10** (2011) 132, doi:10.1007/JHEP10(2011)132, arXiv:1107.4789.

[38] A. Bodek et al., "Extracting Muon Momentum Scale Corrections for Hadron Collider Experiments", *Eur. Phys. J.* **C72** (2012) 2194, doi:10.1140/epjc/s10052-012-2194-8, arXiv:1208.3710.

[39] J. Alwall et al., "The automated computation of tree-level and next-to-leading order differential cross sections, and their matching to parton shower simulations", *JHEP* **07** (2014) 079, doi:10.1007/JHEP07(2014)079, arXiv:1405.0301.

[40] T. Sjöstrand et al., "An introduction to PYTHIA 8.2", *Comput. Phys. Commun.* **191** (2015) 159, doi:10.1016/j.cpc.2015.01.024, arXiv:1410.3012.

[41] NNPDF Collaboration, "Parton distributions for the LHC Run II", *JHEP* **04** (2015) 040, doi:10.1007/JHEP04(2015)040, arXiv:1410.8849.

[42] CMS Collaboration, "Event generator tunes obtained from underlying event and multiparton scattering measurements", *Eur. Phys. J.* **C76** (2016), no. 3, 155, doi:10.1140/epjc/s10052-016-3988-x, arXiv:1512.00815.

[43] NNPDF Collaboration, "Parton distributions with LHC data", *Nucl. Phys. B* **867** (2013) 244, doi:10.1016/j.nuclphysb.2012.10.003, arXiv:1207.1303.

[44] J. Alwall, S. de Visscher, and F. Maltoni, "QCD radiation in the production of heavy colored particles at the LHC", *JHEP* **02** (2009) 017, doi:10.1088/1126-6708/2009/02/017, arXiv:0810.5350.

[45] R. Frederix and S. Frixione, "Merging meets matching in MC@NLO", *JHEP* **12** (2012) 061, doi:10.1007/JHEP12(2012)061, arXiv:1209.6215.

[46] R. Frederix et al., "Four-lepton production at hadron colliders: aMC@NLO predictions with theoretical uncertainties", *JHEP* **02** (2012) 099, doi:10.1007/JHEP02(2012)099, arXiv:1110.4738.

[47] I. V. Tikhonov, "Solution of incorrectly formulated problems and the regularization method", *Soviet Mathematics* **4** (1963), no. 1, 1023–1038.

[48] S. Schmitt, "TUnfold, an algorithm for correcting migration effects in high energy physics", *Journal of Instrumentation* **7** (oct, 2012) T10003–T10003, doi:10.1088/1748-0221/7/10/t10003.

[49] D. Calvetti, L. Reichel, and A. Shuibi, "L-Curve and Curvature Bounds for Tikhonov Regularization", *Numerical Algorithms* **35** (Jan, 2004) 301–314, doi:10.1023/B:NUMA.0000021764.16526.47.

[50] CMS Collaboration, "CMS Luminosity Measurements for the 2016 Data Taking Period", Technical Report CMS-PAS-LUM-17-001, CERN, Geneva, 2017.

[51] L. Lyons, D. Gibaut, and P. Clifford, "How to Combine Correlated Estimates of a Single Physical Quantity", *Nucl. Instrum. Meth.* **A270** (1988) 110, doi:10.1016/0168-9002(88)90018-6.

[52] A. Valassi, "Combining correlated measurements of several different physical quantities", *Nucl. Instrum. Meth.* **A500** (2003) 391–405, doi:10.1016/S0168-9002(03)00329-2.